

Separable Dorsal Raphe Dopamine Projections Mediate Sociability and Valence

Kay Tye (✉ tye@salk.edu)

Salk Institute <https://orcid.org/0000-0002-2435-0182>

Gillian Matthews

<https://orcid.org/0000-0001-6754-0333>

Mackenzie Lemieux

Salk Institute

Elizabeth Brewer

Salk Institute

Raymundo Miranda

Salk Institute

Matilde Borio

Salk Institute

Enzo Peroni

Institut Pasteur <https://orcid.org/0000-0001-7567-1499>

Laurel Keyes

Salk Institute

Grace Pereira

Salk Institute

Alba López Moraga

Salk Institute <https://orcid.org/0000-0002-2084-4855>

Eyal Kimchi

Salk Institute

Nancy Padilla-Coreano

Salk Institute for Biological Studies <https://orcid.org/0000-0001-9293-2697>

Romy Wichmann

Salk Institute

Anna Palle

Salk Institute

Christopher Lee

Salk Institute

Keywords:

Posted Date: December 3rd, 2021

DOI: <https://doi.org/10.21203/rs.3.rs-1025403/v1>

License:  This work is licensed under a Creative Commons Attribution 4.0 International License.

[Read Full License](#)

1 Separable Dorsal Raphe Dopamine Projections Mediate Sociability and Valence

2

3 ^{1,2,3,*}Gillian A. Matthews, ^{1,2,3}Mackenzie E. Lemieux, ²Elizabeth M. Brewer, ^{1,2}Matilde Borio, ^{1,2}Raymundo
4 Miranda, ¹Laurel Keyes, ²Enzo Peroni, ²Grace S. Pereira, ²Alba Lopez Moraga, ²Anna Pallé,
5 ^{1,4}Christopher R. Lee, ²Eyal Y. Kimchi, ^{1,2}Nancy Padilla-Coreano, ^{1,2}Romy Wichmann, ^{1,2,4,*}Kay M. Tye

6

7 ¹Salk Institute for Biological Studies, 10010 N Torrey Pines Rd, La Jolla, CA 92037, USA.

8 ²The Picower Institute for Learning and Memory, Department of Brain and Cognitive Sciences,
9 Massachusetts Institute of Technology, Cambridge, MA 02139, USA.

10 ³Co-first author.

11 ⁴Neurosciences Graduate Program, University of California San Diego, La Jolla, CA 92093, USA

12 *To Whom Correspondence Should be Addressed: g.a.c.matthews@gmail.com (G.A.M.),
13 tye@salk.edu (K.M.T.).

14

15

16 **Abstract**

17 Affiliative social connections facilitate well-being and survival in numerous species. Engaging in
18 social interactions requires positive and negative motivational drive, elicited through coordinated activity
19 across neural circuits. However, the identity, interconnectivity, and functional encoding of social
20 information within these circuits remains poorly understood. Here, we focused on downstream
21 projections of dorsal raphe nucleus (DRN) dopamine neurons (DRN^{DAT}), which we previously implicated
22 in ‘negative drive’-induced social motivation. We show that three prominent DRN^{DAT} projections – to the
23 bed nucleus of the stria terminalis (BNST), central amygdala (CeA), and posterior basolateral amygdala
24 (BLP) – play separable roles in behavior, despite substantial collateralization. Photoactivation of the
25 DRN^{DAT}-CeA projection promoted social behavior and photoactivation of the DRN^{DAT}-BNST projection
26 promoted exploratory behavior, while the DRN^{DAT}-BLP projection supported place avoidance,
27 suggesting a negative affective state. Downstream regions showed diverse, region-specific, receptor
28 expression, poising DRN^{DAT} neurons to act through dopamine, neuropeptide, and glutamate
29 transmission. Furthermore, we show *ex vivo* that the effect of DRN^{DAT} photostimulation on downstream
30 neuron excitability was predicted by baseline cell properties, suggesting cell-type-specific modulation.
31 Collectively, these data indicate that DRN^{DAT} neurons may bias behavior via precise modulation of
32 cellular activity in broadly-distributed target structures.

33

34 **Introduction**

35 A close social network confers a survival advantage, both in the wild and in the laboratory¹⁻³. In
36 humans, objective or subjective isolation (loneliness) increases mortality to levels comparable to
37 smoking or obesity⁴⁻⁶. However, in the short-term, loneliness is theorized to serve an adaptive, survival-
38 promoting function, by encouraging social re-connection and self-preservation⁷. This suggests that
39 underlying neural substrates can detect, evaluate, and rectify imbalances in social connection:
40 potentially operating in a homeostatic manner⁸. Uncovering the identity and operation of these neural
41 circuits is key to understanding our fundamental need for social connection and the neurobiological
42 adaptations associated with social deficit^{9,10}.

43 In pursuit of candidate circuitry, we previously proposed that dopamine neurons within the dorsal
44 raphe nucleus marked by the dopamine transporter (DRN^{DAT}) are sensitive to social isolation and can
45 motivate sociability¹¹. We showed that acute social isolation potentiates glutamatergic synapses onto
46 DRN^{DAT} neurons and augments their population activity on initial social contact. Strikingly, an analogous
47 endeavor in humans similarly revealed that 10 hr of social isolation heightened midbrain responses to
48 social stimuli¹². In mice, we further demonstrated that photostimulation of DRN^{DAT} neurons promoted
49 social preference, but also induced place avoidance, suggesting an underlying negative affective state
50¹¹. This led us to infer a role for these neurons in motivating social approach, driven by the desire to
51 quell a negative state¹³.

52 However, the question remains: how do these neurons simultaneously motivate social approach
53 while also inducing a negative affective state? Other studies have shown that, in non-social contexts,
54 DRN^{DAT} neurons can promote arousal^{14,15}, incentive memory expression¹⁶, antinociception^{17,18}, and
55 fear responses¹⁹. Taken together, this suggests a broad functional role for these neurons in motivating
56 adaptive, survival-promoting behaviors under social and non-social conditions. There are several circuit
57 motifs/neural encoding strategies which could enable this multiplicity of functions: for example distinct
58 functional roles may be associated with projection-defined subpopulations (e.g.²⁰⁻²⁶), neurons may
59 simultaneously encode multiple types of information i.e. show 'mixed selectivity'^{27,28}, or behavioral
60 output may be governed by context- or state-dependency (e.g.²⁹⁻³²). Yet, the mechanisms through
61 which DRN^{DAT} neurons exert their influence over social behavior has yet to be unraveled.

62 Here, we addressed the question of how DRN^{DAT} neurons modulate both sociability and affective
63 state, by exploring the functional role of distinct DRN^{DAT} projections in mice. We show that discrete
64 DRN^{DAT} projections play separable roles in behavior, in spite of their heavily-collateralizing anatomical
65 arrangement. Downstream, we find that within DRN^{DAT} terminal fields, there is spatial segregation of
66 dopamine and neuropeptide receptor expression. Furthermore, photostimulation of DRN^{DAT} inputs can
67 modulate downstream neuronal excitability in a cell-type-specific manner. These findings highlight the
68 anatomical and functional heterogeneity that exists at multiple levels within the DRN^{DAT} system. We
69 suggest this organization may underlie the capacity of the DRN^{DAT} system to exert a broad influence
70 over different forms of behavior: allowing coordinated control over downstream neuronal activity, on
71 distinct timescales, and within disparate target regions.

72 **RESULTS**

73

74 **DRN^{DAT} neurons project to distinct subregions of the amygdala and extended amygdala.**

75 To explore the circuit motifs³³ and computational implementation³⁴ through which the DRN^{DAT}
76 system might operate, we examined whether discrete DRN^{DAT} projections underlie distinct features of
77 behavior. Prominent DRN^{DAT} projections were identified by quantifying downstream fluorescence
78 following Cre-dependent expression of eYFP in dopamine transporter (DAT)::IRES-Cre mice^{11,35–37} (Fig.
79 S1a-d). We observed distinct patterns of innervation arising from ventral tegmental area (VTA)^{DAT} and
80 DRN^{DAT} subpopulations (Fig. S1e-h), with DRN^{DAT} projections most densely targeting the oval nucleus
81 of the BNST (ovBNST) and lateral nucleus of the central amygdala (CeL), with weaker, but significant,
82 input to the posterior part of the basolateral amygdala (BLP), consistent with previous tracing studies
83^{16,36,38–40}. Given that the extended amygdala and basolateral amygdala complex have been implicated
84 in aversion-^{41–44} and reward-related processes^{24,45–47}, and can elicit autonomic and behavioral
85 changes⁴³, we focused on these DRN^{DAT} projections (Fig. S1h).

86

87 **Sociability and aversion are mediated by separable DRN^{DAT} projections.**

88 We next considered whether DRN^{DAT} projections to the BNST, CeA, and BLP play separable or
89 overlapping roles in modulating behavior. Dopaminergic input to the BNST and CeA has been
90 implicated in threat discrimination^{48,49}, anxiety-related behavior⁵⁰, and drug-induced reward^{51–54}, while
91 in the BLA complex, dopamine signaling supports both fear^{55–58} and reward learning^{59,60}. However, the
92 question remains: which DRN^{DAT} projections can influence sociability, and which carry valence-related
93 information?

94 To test the hypothesis that distinct DRN^{DAT} projections promote sociability and induce place
95 avoidance¹¹, we performed projection-specific ChR2-mediated photostimulation. We injected an AAV
96 enabling Cre-dependent expression of ChR2 into the DRN of DAT::Cre male mice, and implanted optic
97 fibers over the BNST, CeA, or BLP (Fig. S2a-c). Given that we previously observed that behavioral
98 effects of DRN^{DAT} photostimulation were predicted by an animal's social rank¹¹, we also assessed
99 relative social dominance using the tube test^{61–63} prior to behavioral assays (Fig. 1a and S2d-e).

100 Firstly, to explore the relationship between social dominance and baseline behavioral profile, we
101 applied a data-driven approach by examining behavioral measures obtained from different assays in a
102 correlation matrix (Fig. S2f). This showed a weak, negative correlation between social dominance and
103 open arm time in the elevated plus maze (EPM) – consistent with a previous report of higher trait anxiety
104 in dominant mice⁶⁴. However, social dominance did not correlate significantly with any other behavioral
105 variable. Furthermore, following dimensionality reduction on baseline behavioral variables, we did not
106 find clearly differentiated clusters of high- and low-ranked mice (Fig. S2g), suggesting that the variation
107 governing these latent features is not related to social rank.

108 Secondly, to assess how projection-specific photostimulation of DRN^{DAT} terminals affected
109 social preference, we used the three-chamber sociability task⁶⁵, where mice freely-explored a chamber
110 containing a novel juvenile mouse and a novel object at opposite ends (Fig. 1b). This revealed that
111 optical stimulation of the DRN^{DAT}-CeA projection increased social preference (Fig. 1c), but no significant
112 effect was observed with photostimulation of either the DRN^{DAT}-BNST or DRN^{DAT}-BLP projections.

113 Furthermore, we found that the optically-induced change in social preference in DRN^{DAT}-CeA mice was
114 positively correlated with social dominance, suggesting that photostimulation elicited a greater increase
115 in sociability in dominant mice (Fig. 1d). This emulates the previous association found with
116 photostimulation at the cell body level ¹¹.

117 Thirdly, we assessed whether photostimulation was sufficient to support place preference using
118 the real-time place-preference (RTPP) assay. Here, we found that photostimulation of the DRN^{DAT}-BLP
119 projection, but not the projection to the BNST or CeA, produced avoidance of the stimulation zone,
120 relative to eYFP controls (Fig. 1e-f). However, we did not find a significant correlation between social
121 dominance and the magnitude of this effect (Fig. 1g). In addition, photostimulation of DRN^{DAT} projections
122 did not have a detectable effect on locomotion (Fig. S3a-c), anxiety-related behavior (Fig. S3d-f), nor
123 operant responding (Fig. S3g-i).

124 Fourthly, to gain further insight into the functional divergence of DRN^{DAT} projections in
125 ethological behaviors, we assessed the effects of photostimulation on social interaction with a novel
126 juvenile in the home-cage (Fig. S2h). Here, photoactivation of the DRN^{DAT}-CeA projection increased
127 face sniffing of the juvenile mouse, consistent with a pro-social role for this projection (Fig. S2i).
128 Contrastingly, photoactivation of the DRN^{DAT}-BNST projection increased rearing behavior (a form of
129 nonsocial exploration ^{66,67}; Fig. S2j-k), an effect that was not previously observed with cell body
130 photostimulation ¹¹. Our analysis of baseline behavioral profile revealed a robust negative correlation
131 between the time spent engaged in social sniffing and time spent rearing (Fig. S2f). When we plotted
132 the difference in face sniffing during photoactivation (i.e. ON-OFF) against the difference in rearing (Fig.
133 S3j-l), we observed that DRN^{DAT}-BNST mice tended to engage in more rearing and less face sniffing
134 during photostimulation (i.e. located in the upper left quadrant) whereas DRN^{DAT}-CeA mice tended to
135 exhibit less rearing and more face sniffing during photostimulation (i.e. located in the lower right
136 quadrant). Finally, to determine whether DRN^{DAT}-CeA photostimulation affected the probability of
137 behavioral state transition ^{68,69}, we examined the sequential structure of behavior using a First-order
138 Markov model ^{69,70}. Considering a 2-state model consisting of 'social' and 'nonsocial' behaviors (Fig.
139 S2l), we found that photostimulation in DRN^{DAT}-CeA mice did not significantly change the probability of
140 transitioning within or between social and nonsocial state (Fig. S2m). This suggests that the DRN^{DAT}-
141 CeA projection may increase engagement in social behavior without altering the overall structure of
142 behavioral transitions.

143 Collectively, these data suggest that DRN^{DAT} projections can exhibit separable functional roles,
144 with the CeA projection promoting sociability and the BLP projection mediating place avoidance.

145

146 **DRN^{DAT} neurons show dense collateralization to extended amygdala targets.**

147 Given the functional separability of distinct DRN^{DAT} projections, we next considered the
148 anatomical organization of these projections to determine whether form gives rise to function. In other
149 words, we investigated whether DRN^{DAT} outputs exhibit a circuit arrangement that facilitates a
150 coordinated behavioral response. Axonal collateralization is one circuit feature that facilitates
151 coordinated activity across broadly distributed structures ⁷¹. Although VTA^{DAT} projections to striatal and
152 cortical regions typically show little evidence of collateralization ⁷²⁻⁷⁶, in contrast, the DRN serotonergic
153 neurons collateralize heavily to innervate the prefrontal cortex, striatum, midbrain, and amygdala ⁷⁷⁻⁷⁹.
154 However, it has yet to be determined whether DRN^{DAT} neurons are endowed with this property.

155 To assess whether DRN^{DAT} neurons exhibit axon collaterals, we performed dual retrograde
156 tracing with fluorophore-conjugated cholera toxin subunit B (CTB)⁸⁰. We injected each tracer into two
157 of the three downstream sites (BNST, CeA, and/or BLP) (Fig. 2a-b and S4a-c) and, after 7 days for
158 retrograde transport, we examined CTB-expressing cells in the DRN that were co-labelled with tyrosine
159 hydroxylase (TH; Fig. 2c-d). CTB injections into the BNST and CeA resulted in numerous TH+ cells
160 labelled with both CTB-conjugated fluorophores, but significantly fewer dual-labelled cells were
161 observed when injections were placed in the BNST and BLP, or CeA and BLP (Fig. 2d-f). These data
162 suggest significant collateralization to the extended amygdala, which includes the BNST and CeA^{16,43}.
163 To confirm the presence of axon collaterals we employed an intersectional viral strategy to selectively
164 label CeA-projecting DRN^{DAT} neurons with cytoplasmic eYFP (Fig. S4d-e). This resulted in eYFP-
165 expressing terminals both in the CeA and in the BNST (Fig. S4f-g).

166 Taken together, this indicates that DRN^{DAT} axons collateralize heavily to innervate the BNST
167 and CeA, with relatively fewer collaterals innervating the BLP. This anatomical architecture may enable
168 DRN^{DAT} projections to achieve coordinated recruitment of distributed neuronal populations⁷¹, that may
169 still be locally modulated within the downstream target.

170

171 **DRN^{DAT} terminal fields contain spatially-segregated dopamine and neuropeptide receptor** 172 **populations.**

173 Our data suggest that DRN^{DAT} projections exert divergent effects over behavior, despite
174 substantial overlap in their upstream cells of origin. Given this overlap, we reasoned that one
175 mechanism through which these projections might achieve distinct behavioral effects is via differential
176 recruitment of downstream signaling pathways. We, therefore, next considered whether the pattern of
177 receptor expression differed within the DRN^{DAT} terminal field of these downstream regions.

178 Subsets of DRN^{DAT} neurons co-express vasoactive intestinal peptide (VIP) and neuropeptide-W
179 (NPW)⁸¹⁻⁸³, and so we examined both dopamine (*Drd1* and *Drd2*) and neuropeptide (*Vipr2* and *Npbwr1*)
180 receptor expression within DRN^{DAT} terminal fields. To achieve this, we performed single molecule
181 fluorescence *in situ* hybridization (smFISH) using RNAscope (Fig. S5a-b). In the BNST and CeA we
182 observed a strikingly similar pattern of receptor expression with dense neuropeptide receptor
183 expression in the oval BNST and ventromedial CeL, and a high degree of co-localization (Fig. 3a-h and
184 S5c-h). In the BNST and CeA subregions containing the highest density of DRN^{DAT} terminals, dopamine
185 receptor expression was relatively more sparse, with *Drd2* more abundant than *Drd1*, as previously
186 described^{47,48,50,84,85} (Fig. 3a-h). The DRN^{DAT} terminal field of the BLP displayed a markedly different
187 receptor expression pattern, dominated by *Drd1* (Fig. 3i-l and S5i-k), consistent with previous reports
188^{50,59,84}. Thus, in contrast to the BNST and CeA, the effects of DRN^{DAT} input to the BLP may be
189 predominantly mediated via D₁-receptor signaling. Collectively, this expression pattern suggests that
190 the dopamine- and neuropeptide-mediated effects of DRN^{DAT} input may be spatially-segregated within
191 downstream regions – providing the infrastructure for divergent modulation of cellular subsets.

192

193

194 **DRN^{DAT} input has divergent effects on downstream cellular excitability.**

195 Our data suggest that DRN^{DAT} projections exert divergent effects over behavior, despite
196 substantial collateralization. One mechanism through which these projections might achieve distinct
197 behavioral effects is via differential modulation of activity in downstream neurons. The multi-transmitter
198 phenotype of DRN^{DAT} neurons^{81,82,86,87}, regionally-distinct downstream receptor expression, and the
199 observed pre- and post-synaptic actions of exogenously applied dopamine^{88–95} provides optimal
200 conditions for diverse modulation of neural activity. However, it remains unknown how temporally
201 precise activation of DRN^{DAT} terminals influences excitability at the single-cell level.

202 We, therefore, next examined how DRN^{DAT} input affects downstream excitability. To achieve
203 this, we expressed ChR2 in DRN^{DAT} neurons, and used *ex vivo* electrophysiology to record from
204 downstream neurons (Fig. 4a-c and S6a-c). Optical stimulation at the resting membrane potential
205 evoked both excitatory and inhibitory post-synaptic potentials (EPSPs and IPSPs) in downstream cells
206 (Fig. 4d-f), which were typically monosynaptic (Fig. S6d-e). During spontaneous firing, BNST cells were
207 excited and BLP cells mostly inhibited by DRN^{DAT} optical stimulation, whereas a mixture of responses
208 was observed in the CeA (Fig. 4g-k and S6f-g). The fast rise and decay kinetics of the EPSP suggest
209 an AMPAR-mediated potential, resulting from glutamate co-release^{11,17}, whereas the slow IPSP
210 kinetics are consistent with opening of GIRK channels, which can occur via D₂-receptor^{96,97} or GABA-
211_B receptor signaling^{98–100}.

212 Given the diversity of responses observed in the CeA and BLP, we next examined these
213 downstream cells in more detail. To assess whether baseline electrophysiological properties predicted
214 the optically-evoked response, we used unsupervised agglomerative hierarchical clustering to classify
215 downstream cells (Fig. 4l-m). This established approach has been successfully applied to
216 electrophysiological datasets to reveal distinct neuronal subclasses^{101–103}. The resulting dendrograms
217 yielded two major clusters in the CeA and BLP, with distinct electrophysiological characteristics (Fig.
218 4n-q and S6h-k). CeA cells in cluster 1 represented ‘late-firing’ neurons, whereas cluster 2 were typical
219 of ‘regular-firing’ neurons^{104–106}. Strikingly, these clusters exhibited dramatically different responses to
220 DRN^{DAT} photostimulation, with cluster 1 ‘late-firing’ neurons excited and cluster 2 ‘regular-firing’ neurons
221 mostly inhibited (Fig. 4o). Similarly, BLP cells delineated into two major clusters, with properties
222 characteristic of pyramidal neurons (cluster 1) and GABAergic interneurons (cluster 2) (Fig. 4p-q).
223 These clusters showed remarkably different responses to DRN^{DAT} input, with 93% of putative pyramidal
224 neurons showing an inhibitory response, and 62% of putative GABAergic interneurons showing an
225 excitatory response (Fig. 4q). In addition, clustering CeA and BLP cells together yielded a very similar
226 result (Fig. S6l-n), perhaps reflecting similar anatomical architecture that can be repurposed towards
227 distinct functions. Thus, while photoactivation of DRN^{DAT} terminals elicits heterogeneous responses in
228 downstream neurons, baseline cell properties strongly predict their response, suggesting robust
229 synaptic organization. The opposing nature of these responses, in different neuronal subsets, suggests
230 that – rather than inducing an overall augmentation or suppression of activity – DRN^{DAT} input may adjust
231 the *pattern* of downstream activity, in order to exert a functional shift in behavior.

232

233

234

235

236 **DISCUSSION**

237 Neural circuits which motivate social approach are essential in maintaining social connections
238 and preventing isolation. Here we show that DRN^{DAT} neurons can exert a multi-faceted influence over
239 behavior, with the pro-social effects mediated by the projection to the CeA. Our data suggest these
240 effects are enabled via separable functional projections, dense collateralization, co-transmission, and
241 precisely organized synaptic connectivity. Taken together, these circuit features may facilitate a
242 coordinated, but flexible, response in the presence of social stimuli, that can be flexibly guided based
243 on internal social homeostatic need state.

244

245 **DRN^{DAT} circuit arrangement enables a broadly distributed, coordinated response.**

246 Our findings revealed several features of the DRN^{DAT} circuit which might facilitate a concerted
247 response to novel social and non-social situations. Firstly, we observed dissociable roles for discrete
248 downstream projections – a common motif of valence-encoding neural circuits³³. Biased recruitment of
249 these ‘divergent paths’³³ to the BNST, CeA, and BLP by upstream inputs may serve to fine-tune the
250 balance between social investigation and environmental exploration: facilitating behavioral flexibility
251 with changing environmental conditions or internal state. Secondly, we demonstrate extensive
252 collateralization of DRN^{DAT} neurons. In other populations, collateralization is proposed to aid temporal
253 coordination of a multifaceted response: enabling synchronous activation of distributed regions^{71,79}.
254 This feature may, therefore, facilitate coordinated recruitment of the BNST and CeA, allowing these
255 regions to work in concert to promote social approach while also maintaining vigilance to salient
256 environmental stimuli. Thirdly we find precise synaptic organization in the DRN^{DAT} modulation of
257 downstream neuronal activity. Combined with the spatially-segregated downstream receptor
258 expression pattern, this organization may allow DRN^{DAT} neurons to elicit broad, yet finely-tuned, control
259 over the pattern of neuronal activity, on multiple timescales.

260

261 **Separable projections mediate social behavior and valence.**

262 Our data supports the hypothesis that separable DRN^{DAT} projections mediate distinct functional
263 roles: a feature which has been previously observed in other neuronal circuits (e.g.^{20–24}). The DRN^{DAT}
264 circuit attributes we describe above may further enable this system to modulate other diverse forms of
265 behavior (e.g. arousal¹⁴, fear/reward associations^{16,19}, and antinociception^{17,18}). These could be
266 mediated via other downstream projections and/or via these same projections under different
267 environmental contexts, testing conditions, and/or internal states. Further work is required to determine
268 how this system is able to exert a broad influence over multiple forms of behavior. Collectively, however,
269 our data and others support a role for the DRN^{DAT} system in exerting a coordinated behavioral response
270 to novel situations – both social and non-social.

271 The CeA has been implicated in mediating the response to threats – orchestrating defensive
272 behavioral responses and autonomic changes via efferents to subcortical and brainstem nuclei^{41,107–}
273¹⁰⁹. One possible interpretation, therefore, is that DRN^{DAT} input to the CeA suppresses fear-promoting
274 neuronal ensembles in order to facilitate social approach. In the maintenance of social homeostasis,
275 suppression of fear in the presence of social stimuli may represent an adaptive response – preventing
276 salient social stimuli from being interpreted as a threat. Indeed, other need states, such as hunger, are
277 associated with fear suppression and higher-risk behavior¹¹⁰, suggesting a conserved response to

278 homeostatic imbalance⁸. However, the motivation to attend to social stimuli may also be driven by
279 territorial defense, highlighting a need to further understand how internal states can play into the output
280 of this system. A more comprehensive knowledge of the functional cell-types modulated by DRN^{DAT}
281 activity will facilitate our understanding of how this input can shape the downstream neuronal
282 representation of social and non-social stimuli.

283 In contrast to the CeA, photoactivation of the DRN^{DAT}-BLP projection produced avoidance of the
284 stimulation zone, suggesting an aversive state. This differs from the valence-independent role of VTA
285 dopamine input to the greater BLA complex, wherein dopamine signaling gates synaptic plasticity for
286 associative learning of both positive and negative valence⁶⁰ and responds to salient stimuli predicting
287 both positive and negative outcomes⁵⁹. However, DRN and VTA axonal fields differ within the BLA
288 complex, with DRN^{DAT} terminals being more concentrated within the BLP, and VTA^{DAT} inputs traversing
289 the LA, BLA and intercalated cells more densely.

290 While there have been seemingly contradictory reports on the effect of dopamine on excitability
291 in the BLA, our observations using photostimulation of DRN^{DAT} terminals (in short phasic bursts) are
292 consistent with *in vivo* extracellular recordings combined with electrical stimulation of the midbrain⁹³.
293 One unifying hypothesis is that dopamine induces an *indirect* GABA-mediated suppression of pyramidal
294 neurons, which may attenuate their response to weak inputs, while *directly* exciting pyramidal neurons
295 to augment their response to large inputs^{90,93}. In this way, amygdala dopamine may underlie a similar
296 role to cortical dopamine¹¹¹: enhancing signal-to-noise ratio to facilitate behavioral responses to salient
297 stimuli¹¹².

298

299 **Multi-transmitter phenotype of DRN^{DAT} neurons may permit modulation on different timescales.**

300 DRN^{DAT} neurons possess an impressive repertoire of signaling molecules: alongside dopamine
301 and glutamate subsets of DRN^{DAT} neuron express VIP and NPW⁸¹⁻⁸³. While there is some partial
302 segregation of VIP- and NPW-expressing neurons⁸², our receptor expression analyses suggest that
303 these neuropeptides converge on the same neurons in the BNST and CeA. This co-localization is
304 intriguing, given that *Vipr2* is typically coupled to the excitatory G_s-protein¹¹³, while *Npbwr1* is coupled
305 to the inhibitory G_i-protein^{114,115}. Therefore, signaling through these receptors may exert opposing
306 actions on downstream cells. Recruitment of neuropeptidergic signaling pathways may support slower,
307 sustained downstream modulation, for example, in hunger-mediating hypothalamic Agouti-Related
308 Peptide (AgRP) neurons, neuropeptide co-release is essential for sustaining feeding behavior¹¹⁶.
309 Therefore, a delayed, persistent neuropeptide-mediated signal might enable downstream modulation
310 to outlive phasic DRN^{DAT} activity: promoting behavioral adjustments over longer timescales.

311 While the functional role of these neuropeptides remains to be elucidated, studies on knockout
312 mice suggest a role for NPW in social behavior and stress responding^{114, 83}. Furthermore, humans with
313 a single-nucleotide polymorphism (SNP) of the *NPBWR1* gene (which impairs receptor function)
314 perceive fearful/angry faces as more positive and less submissive¹¹⁷, indicating a role for NPW
315 signaling in interpreting social signals. Similarly, the function of DRN VIP+ neurons has received little
316 attention in rodent models, but there has been more focus on the role of VIP in avian social behavior
317¹¹⁸. Of particular interest, in the rostral arcopallium (a homolog of mammalian amygdala¹¹⁹), VIP binding
318 density is elevated in birds during seasonal flocking¹²⁰. This suggests that elevated VIP receptor
319 expression may encourage affiliative social grouping behavior in birds¹²⁰. Thus, NPW and VIP may act

320 in concert with fast glutamate-mediated and slow dopamine-mediated neurotransmission in the central
321 extended amygdala, to modulate behavior on different timescales.

322

323 **Conclusion**

324 Our findings support a role for DRN^{DAT} projections in promoting distinct features of the response
325 to novel social stimuli – orchestrating a coordinated, flexible response through recruitment of specific
326 downstream circuits. This highlights the breadth of DRN^{DAT} influence over downstream targets, the
327 signaling complexity of this system, and its potential to underlie a shift in both behavior and affective
328 state. Uncovering the neural circuit mechanisms which incline individuals towards sociability is key to
329 understanding the basic human need for social connection and the neural representation of loneliness.

330

331

332 **ACKNOWLEDGEMENTS**

333 K.M.T. is the Wylie Vale Chair at the Salk Institute for Biological Studies, a New York Stem Cell
334 Foundation - Robertson Investigator, and a McKnight Scholar. This work was supported by funding from
335 the JPB Foundation, Alfred P Sloan Foundation, New York Stem Cell Foundation, Klingenstein
336 Foundation, McKnight Foundation, Clayton Foundation, Dolby Family Fund, R01-MH115920 (NIMH),
337 the NIH Director's New Innovator Award DP2-DK102256 (NIDDK), and Pioneer Award DP1-AT009925
338 (NCCIH). G.A.M was supported by a Postdoctoral Research Fellowship from the Charles A. King Trust.
339 R.L.M. was funded through the MSRP program in the Brains & Cognitive Sciences Department at MIT,
340 supported by the Center for Brains, Minds and Machines (CBMM), and funded by NSF STC award
341 CCF-1231216. E.M.B was supported by a summer scholarship from Johnson & Johnson. We thank C.
342 Leppla, J. Olsen, P. Namburi, V. Barth, J. Wang, K. Batra, A. Brown, and A. Libster for technical advice,
343 all members of the Tye Lab for helpful discussion, and advice from the CellProfiler team at the Broad
344 Institute. We also thank Rachel Neve for the HSV construct, and Charu Ramakrishnan & Karl Deisseroth
345 for AAV₅-fDIO-eYFP.

346

347 **AUTHOR CONTRIBUTIONS**

348 K.M.T. and G.A.M. conceptualized the project, designed experiments, supervised experiments, and
349 directed data analyses. M.E.L and M.B. performed and analyzed smFISH experiments. G.A.M., M.E.L.,
350 C.R.L., E.M.B., E.P., G.S.P., A.L.M., and A.P.L. performed stereotaxic surgeries. G.A.M., E.M.B, E.P,
351 G.S.P, M.E.L., M.B., A.L.M, R.M., C.R.L., and A.P.L. ran optogenetic manipulation experiments and
352 analyzed behavioral data. L.K. performed Markov model analysis. G.A.M., E.M.B., E.P., G.S.P., A.L.M.,
353 and A.P.L. performed immunohistochemistry and analyzed images. G.A.M performed *ex vivo*
354 electrophysiology, and N.P-C., E.Y.K, and R.W. contributed to experimental design and data
355 interpretation. G.A.M. and K.M.T. wrote the manuscript with review and editing from M.E.L., C.R.L.,
356 E.M.B., M.B., R.M., L.K., E.P., G.S.P., A.L.M., A.P.L., E.Y.K., N.P-C., and R.W.

357

358 **REFERENCES**

- 359 1. Koto, A., Mersch, D., Hollis, B. & Keller, L. Social isolation causes mortality by disrupting energy
360 homeostasis in ants. *Behav. Ecol. Sociobiol.* **69**, 583–591 (2015).
- 361 2. Silk, J. B. *et al.* Strong and Consistent Social Bonds Enhance the Longevity of Female Baboons. *Curr. Biol.*
362 **20**, 1359–1361 (2010).
- 363 3. Yee, J. R., Cavigelli, S. A., Delgado, B. & McClintock, M. K. Reciprocal affiliation among adolescent rats
364 during a mild group stressor predicts mammary tumors and lifespan. *Psychosom. Med.* **70**, 1050–1059
365 (2008).
- 366 4. Holt-Lunstad, J., Smith, T. B. & Layton, J. B. Social Relationships and Mortality Risk: A Meta-analytic
367 Review. *PLoS Med* **7**, e1000316 (2010).
- 368 5. Holt-Lunstad, J., Smith, T. B., Baker, M., Harris, T. & Stephenson, D. Loneliness and social isolation as risk
369 factors for mortality: a meta-analytic review. *Perspect. Psychol. Sci. J. Assoc. Psychol. Sci.* **10**, 227–237
370 (2015).
- 371 6. Pantell, M. *et al.* Social Isolation: A Predictor of Mortality Comparable to Traditional Clinical Risk Factors.
372 *Am. J. Public Health* **103**, 2056–2062 (2013).
- 373 7. Cacioppo, J. T. & Cacioppo, S. Chapter Three - Loneliness in the Modern Age: An Evolutionary Theory of
374 Loneliness (ETL). in *Advances in Experimental Social Psychology* (ed. Olson, J. M.) vol. 58 127–197
375 (Academic Press, 2018).
- 376 8. Matthews, G. A. & Tye, K. M. Neural mechanisms of social homeostasis. *Ann. N. Y. Acad. Sci.* **1457**, 5–25
377 (2019).
- 378 9. Lee, C. R., Chen, A. & Tye, K. M. The neural circuitry of social homeostasis: Consequences of acute versus
379 chronic social isolation. *Cell* **184**, 1500–1516 (2021).
- 380 10. Tomova, L., Tye, K. & Saxe, R. The neuroscience of unmet social needs. *Soc. Neurosci.* **0**, 1–11 (2019).
- 381 11. Matthews, G. A. *et al.* Dorsal Raphe Dopamine Neurons Represent the Experience of Social Isolation. *Cell*
382 **164**, 617–631 (2016).

- 383 12. Tomova, L. *et al.* Acute social isolation evokes midbrain craving responses similar to hunger. *Nat.*
384 *Neurosci.* **23**, 1597–1605 (2020).
- 385 13. Hull, C. L. *Principles of Behavior: An Introduction to Behavior Theory.* (D. Appleton-Century Company,
386 Incorporated, 1943).
- 387 14. Cho, J. R. *et al.* Dorsal Raphe Dopamine Neurons Modulate Arousal and Promote Wakefulness by Salient
388 Stimuli. *Neuron* **94**, 1205-1219.e8 (2017).
- 389 15. Lu, J., Zhou, T. C. & Saper, C. B. Identification of wake-active dopaminergic neurons in the ventral
390 periaqueductal gray matter. *J. Neurosci. Off. J. Soc. Neurosci.* **26**, 193–202 (2006).
- 391 16. Lin, R. *et al.* The Raphe Dopamine System Controls the Expression of Incentive Memory. *Neuron* **106**,
392 498-514.e8 (2020).
- 393 17. Li, C. *et al.* Mu Opioid Receptor Modulation of Dopamine Neurons in the Periaqueductal Gray/Dorsal
394 Raphe: A Role in Regulation of Pain. *Neuropsychopharmacol. Off. Publ. Am. Coll. Neuropsychopharmacol.*
395 **41**, 2122–2132 (2016).
- 396 18. Meyer, P. J., Morgan, M. M., Kozell, L. B. & Ingram, S. L. Contribution of dopamine receptors to
397 periaqueductal gray-mediated antinociception. *Psychopharmacology (Berl.)* **204**, 531–540 (2009).
- 398 19. Groessl, F. *et al.* Dorsal tegmental dopamine neurons gate associative learning of fear. *Nat. Neurosci.* **21**,
399 952–962 (2018).
- 400 20. Han, W. *et al.* Integrated Control of Predatory Hunting by the Central Nucleus of the Amygdala. *Cell* **168**,
401 311-324.e18 (2017).
- 402 21. Kim, S.-Y. *et al.* Diverging neural pathways assemble a behavioural state from separable features in
403 anxiety. *Nature* **496**, 219–223 (2013).
- 404 22. Kohl, J. *et al.* Functional circuit architecture underlying parental behaviour. *Nature* **556**, 326–331 (2018).
- 405 23. Lammel, S., Ion, D. I., Roeper, J. & Malenka, R. C. Projection-specific modulation of dopamine neuron
406 synapses by aversive and rewarding stimuli. *Neuron* **70**, 855–862 (2011).

- 407 24. Namburi, P. *et al.* A circuit mechanism for differentiating positive and negative associations. *Nature* **520**,
408 675–678 (2015).
- 409 25. Senn, V. *et al.* Long-Range Connectivity Defines Behavioral Specificity of Amygdala Neurons. *Neuron* **81**,
410 428–437 (2014).
- 411 26. Tye, K. M. *et al.* Amygdala circuitry mediating reversible and bidirectional control of anxiety. *Nature* **471**,
412 358–362 (2011).
- 413 27. Rigotti, M. *et al.* The importance of mixed selectivity in complex cognitive tasks. *Nature* **497**, 585–590
414 (2013).
- 415 28. Tian, J. *et al.* Distributed and Mixed Information in Monosynaptic Inputs to Dopamine Neurons. *Neuron*
416 **91**, 1374–1389 (2016).
- 417 29. Krzywkowski, P., Penna, B. & Gross, C. T. Dynamic encoding of social threat and spatial context in the
418 hypothalamus. *eLife* **9**, e57148 (2020).
- 419 30. Kyriazi, P., Headley, D. B. & Pare, D. Multi-dimensional Coding by Basolateral Amygdala Neurons. *Neuron*
420 **99**, 1315-1328.e5 (2018).
- 421 31. Lemos, J. C. *et al.* Severe stress switches CRF action in the nucleus accumbens from appetitive to
422 aversive. *Nature* **490**, 402–406 (2012).
- 423 32. Seo, C. *et al.* Intense Threat Switches Dorsal Raphe Serotonin Neurons to a Paradoxical Operational
424 Mode. *Science* **363**, 538–542 (2019).
- 425 33. Tye, K. M. Neural Circuit Motifs in Valence Processing. *Neuron* **100**, 436–452 (2018).
- 426 34. Lockwood, P. L., Apps, M. A. J. & Chang, S. W. C. Is There a ‘Social’ Brain? Implementations and
427 Algorithms. *Trends Cogn. Sci.* **24**, 802–813 (2020).
- 428 35. Bäckman, C. M. *et al.* Characterization of a mouse strain expressing Cre recombinase from the 3’
429 untranslated region of the dopamine transporter locus. *Genes. N. Y. N* **2000** **44**, 383–390 (2006).
- 430 36. Cardozo Pinto, D. F. *et al.* Characterization of transgenic mouse models targeting neuromodulatory
431 systems reveals organizational principles of the dorsal raphe. *Nat. Commun.* **10**, 4633 (2019).

- 432 37. Lammel, S. *et al.* Diversity of transgenic mouse models for selective targeting of midbrain dopamine
433 neurons. *Neuron* **85**, 429–438 (2015).
- 434 38. Hasue, R. H. & Shammah-Lagnado, S. J. Origin of the dopaminergic innervation of the central extended
435 amygdala and accumbens shell: a combined retrograde tracing and immunohistochemical study in the
436 rat. *J. Comp. Neurol.* **454**, 15–33 (2002).
- 437 39. Meloni, E. G., Gerety, L. P., Knoll, A. T., Cohen, B. M. & Carlezon, W. A. Behavioral and Anatomical
438 Interactions between Dopamine and Corticotropin-Releasing Factor in the Rat. *J. Neurosci.* **26**, 3855–
439 3863 (2006).
- 440 40. Oh, S. W. *et al.* A mesoscale connectome of the mouse brain. *Nature* **508**, 207–214 (2014).
- 441 41. Davis, M., Walker, D. L., Miles, L. & Grillon, C. Phasic vs Sustained Fear in Rats and Humans: Role of the
442 Extended Amygdala in Fear vs Anxiety. *Neuropsychopharmacology* **35**, 105–135 (2010).
- 443 42. Goode, T. D. & Maren, S. Role of the bed nucleus of the stria terminalis in aversive learning and memory.
444 *Learn. Mem.* **24**, 480–491 (2017).
- 445 43. Janak, P. H. & Tye, K. M. From circuits to behaviour in the amygdala. *Nature* **517**, 284–292 (2015).
- 446 44. Lebow, M. A. & Chen, A. Overshadowed by the amygdala: the bed nucleus of the stria terminalis emerges
447 as key to psychiatric disorders. *Mol. Psychiatry* **21**, 450–463 (2016).
- 448 45. Douglass, A. M. *et al.* Central amygdala circuits modulate food consumption through a positive-valence
449 mechanism. *Nat. Neurosci.* **20**, 1384–1394 (2017).
- 450 46. Jennings, J. H. *et al.* Distinct extended amygdala circuits for divergent motivational states. *Nature* **496**,
451 224–228 (2013).
- 452 47. Kim, J., Zhang, X., Muralidhar, S., LeBlanc, S. A. & Tonegawa, S. Basolateral to Central Amygdala Neural
453 Circuits for Appetitive Behaviors. *Neuron* **93**, 1464–1479.e5 (2017).
- 454 48. De Bundel, D. *et al.* Dopamine D2 receptors gate generalization of conditioned threat responses through
455 mTORC1 signaling in the extended amygdala. *Mol. Psychiatry* **21**, 1545–1553 (2016).

- 456 49. Jo, Y. S., Heymann, G. & Zweifel, L. S. Dopamine Neurons Reflect the Uncertainty in Fear Generalization.
457 *Neuron* **100**, 916-925.e3 (2018).
- 458 50. Perez de la Mora, M. *et al.* Distribution of dopamine D(2)-like receptors in the rat amygdala and their role
459 in the modulation of unconditioned fear and anxiety. *Neuroscience* **201**, 252–266 (2012).
- 460 51. Eiler, W. J. A., Seyoum, R., Foster, K. L., Mailey, C. & June, H. L. D1 dopamine receptor regulates alcohol-
461 motivated behaviors in the bed nucleus of the stria terminalis in alcohol-preferring (P) rats. *Synap. N. Y. N*
462 **48**, 45–56 (2003).
- 463 52. Epping-Jordan, M. P., Markou, A. & Koob, G. F. The dopamine D-1 receptor antagonist SCH 23390
464 injected into the dorsolateral bed nucleus of the stria terminalis decreased cocaine reinforcement in the
465 rat. *Brain Res.* **784**, 105–115 (1998).
- 466 53. Rezayof, A., Zarrindast, M.-R., Sahraei, H. & Haeri-Rohani, A.-H.-R. Involvement of dopamine D2 receptors
467 of the central amygdala on the acquisition and expression of morphine-induced place preference in rat.
468 *Pharmacol. Biochem. Behav.* **74**, 187–197 (2002).
- 469 54. Thiel, K. J. *et al.* Stimulation of dopamine D2/D3 but not D1 receptors in the central amygdala decreases
470 cocaine-seeking behavior. *Behav. Brain Res.* **214**, 386–394 (2010).
- 471 55. Bissière, S., Humeau, Y. & Luthi, A. Dopamine gates LTP induction in lateral amygdala by suppressing
472 feedforward inhibition. *Nat. Neurosci.* **6**, 587–592 (2003).
- 473 56. Fadok, J. P., Dickerson, T. M. K. & Palmiter, R. D. Dopamine Is Necessary for Cue-Dependent Fear
474 Conditioning. *J. Neurosci.* **29**, 11089–11097 (2009).
- 475 57. Guarraci, F. A., Frohardt, R. J. & Kapp, B. S. Amygdaloid D1 dopamine receptor involvement in Pavlovian
476 fear conditioning. *Brain Res.* **827**, 28–40 (1999).
- 477 58. de Oliveira, A. R. *et al.* Conditioned fear is modulated by D2 receptor pathway connecting the ventral
478 tegmental area and basolateral amygdala. *Neurobiol. Learn. Mem.* **95**, 37–45 (2011).
- 479 59. Lutas, A. *et al.* State-specific gating of salient cues by midbrain dopaminergic input to basal amygdala.
480 *Nat. Neurosci.* **22**, 1820–1833 (2019).

- 481 60. Tye, K. M. *et al.* Methylphenidate facilitates learning-induced amygdala plasticity. *Nat. Neurosci.* **13**, 475–
482 481 (2010).
- 483 61. Lindzey, G., Winston, H. & Manosevitz, M. Social Dominance in Inbred Mouse Strains. *Nature* **191**, 474–
484 476 (1961).
- 485 62. Wang, F. *et al.* Bidirectional Control of Social Hierarchy by Synaptic Efficacy in Medial Prefrontal Cortex.
486 *Science* **334**, 693–697 (2011).
- 487 63. Zhou, T., Sandi, C. & Hu, H. Advances in understanding neural mechanisms of social dominance. *Curr.*
488 *Opin. Neurobiol.* **49**, 99–107 (2018).
- 489 64. Larrieu, T. *et al.* Hierarchical Status Predicts Behavioral Vulnerability and Nucleus Accumbens Metabolic
490 Profile Following Chronic Social Defeat Stress. *Curr. Biol.* **27**, 2202-2210.e4 (2017).
- 491 65. Moy, S. S. *et al.* Sociability and preference for social novelty in five inbred strains: an approach to assess
492 autistic-like behavior in mice. *Genes Brain Behav.* **3**, 287–302 (2004).
- 493 66. Bailey, K. R. & Crawley, J. N. Anxiety-Related Behaviors in Mice. in *Methods of Behavior Analysis in*
494 *Neuroscience* (ed. Buccafusco, J. J.) (CRC Press/Taylor & Francis, 2009).
- 495 67. Lever, C., Burton, S. & O’Keefe, J. Rearing on hind legs, environmental novelty, and the hippocampal
496 formation. *Rev. Neurosci.* **17**, 111–133 (2006).
- 497 68. Füzési, T., Daviu, N., Wamsteeker Cusulin, J. I., Bonin, R. P. & Bains, J. S. Hypothalamic CRH neurons
498 orchestrate complex behaviours after stress. *Nat. Commun.* **7**, 11937 (2016).
- 499 69. Lee, W., Fu, J., Bouwman, N., Farago, P. & Curley, J. P. Temporal microstructure of dyadic social behavior
500 during relationship formation in mice. *PLoS ONE* **14**, (2019).
- 501 70. Tejada, J., Bosco, G. G., Morato, S. & Roque, A. C. Characterization of the rat exploratory behavior in the
502 elevated plus-maze with Markov chains. *J. Neurosci. Methods* **193**, 288–295 (2010).
- 503 71. Rockland, K. S. Axon Collaterals and Brain States. *Front. Syst. Neurosci.* **12**, (2018).

- 504 72. Aransay, A., Rodríguez-López, C., García-Amado, M., Clascá, F. & Prensa, L. Long-range projection
505 neurons of the mouse ventral tegmental area: a single-cell axon tracing analysis. *Front. Neuroanat.* **9**,
506 (2015).
- 507 73. Beier, K. T. *et al.* Circuit Architecture of VTA Dopamine Neurons Revealed by Systematic Input–Output
508 Mapping. *Cell* **162**, 622–634 (2015).
- 509 74. Lerner, T. N. *et al.* Intact-Brain Analyses Reveal Distinct Information Carried by SNc Dopamine Subcircuits.
510 *Cell* **162**, 635–647 (2015).
- 511 75. Matsuda, W. *et al.* Single Nigrostriatal Dopaminergic Neurons Form Widely Spread and Highly Dense
512 Axonal Arborizations in the Neostriatum. *J. Neurosci.* **29**, 444–453 (2009).
- 513 76. Moore, R. Y. & Bloom, F. E. Central catecholamine neuron systems: anatomy and physiology of the
514 dopamine systems. *Annu. Rev. Neurosci.* **1**, 129–169 (1978).
- 515 77. Gagnon, D. & Parent, M. Distribution of VGLUT3 in Highly Collateralized Axons from the Rat Dorsal Raphe
516 Nucleus as Revealed by Single-Neuron Reconstructions. *PLOS ONE* **9**, e87709 (2014).
- 517 78. van der Kooy, D. & Hattori, T. Dorsal raphe cells with collateral projections to the caudate-putamen and
518 substantia nigra: a fluorescent retrograde double labeling study in the rat. *Brain Res.* **186**, 1–7 (1980).
- 519 79. Waselus, M., Valentino, R. J. & Van Bockstaele, E. J. Collateralized dorsal raphe nucleus projections: a
520 mechanism for the integration of diverse functions during stress. *J. Chem. Neuroanat.* **41**, 266–280
521 (2011).
- 522 80. Beyeler, A. *et al.* Organization of Valence-Encoding and Projection-Defined Neurons in the Basolateral
523 Amygdala. *Cell Rep.* **22**, 905–918 (2018).
- 524 81. Dougalis, A. G. *et al.* Functional properties of dopamine neurons and co-expression of vasoactive
525 intestinal polypeptide in the dorsal raphe nucleus and ventro-lateral periaqueductal grey. *Eur. J.*
526 *Neurosci.* **36**, 3322–3332 (2012).
- 527 82. Huang, K. W. *et al.* Molecular and anatomical organization of the dorsal raphe nucleus. *eLife* **8**, e46464
528 (2019).

- 529 83. Motoike, T. *et al.* Mesolimbic neuropeptide W coordinates stress responses under novel environments.
530 *Proc. Natl. Acad. Sci. U. S. A.* **113**, 6023–6028 (2016).
- 531 84. McCullough, K. M., Daskalakis, N. P., Gafford, G., Morrison, F. G. & Ressler, K. J. Cell-type-specific
532 interrogation of CeA Drd2 neurons to identify targets for pharmacological modulation of fear extinction.
533 *Transl. Psychiatry* **8**, (2018).
- 534 85. McCullough, K. M., Morrison, F. G., Hartmann, J., Carlezon, W. A. & Ressler, K. J. Quantified Coexpression
535 Analysis of Central Amygdala Subpopulations. *eNeuro* **5**, (2018).
- 536 86. Dougalis, A. G., Matthews, G. A. C., Liss, B. & Ungless, M. A. Ionic currents influencing spontaneous firing
537 and pacemaker frequency in dopamine neurons of the ventrolateral periaqueductal gray and dorsal
538 raphe nucleus (vlPAG/DRN): A voltage-clamp and computational modelling study. *J. Comput. Neurosci.*
539 **42**, 275–305 (2017).
- 540 87. Poulin, J.-F. *et al.* Mapping projections of molecularly defined dopamine neuron subtypes using
541 intersectional genetic approaches. *Nat. Neurosci.* **21**, 1260–1271 (2018).
- 542 88. Kash, T. L., Nobis, W. P., Matthews, R. T. & Winder, D. G. Dopamine Enhances Fast Excitatory Synaptic
543 Transmission in the Extended Amygdala by a CRF-R1-Dependent Process. *J. Neurosci.* **28**, 13856–13865
544 (2008).
- 545 89. Krawczyk, M. *et al.* Double-Dissociation of the Catecholaminergic Modulation of Synaptic Transmission in
546 the Oval Bed Nucleus of the Stria Terminalis. *J. Neurophysiol.* **105**, 145–153 (2010).
- 547 90. Kröner, S., Rosenkranz, J. A., Grace, A. A. & Barrionuevo, G. Dopamine Modulates Excitability of
548 Basolateral Amygdala Neurons In Vitro. *J. Neurophysiol.* **93**, 1598–1610 (2005).
- 549 91. Marowsky, A., Yanagawa, Y., Obata, K. & Vogt, K. E. A Specialized Subclass of Interneurons Mediates
550 Dopaminergic Facilitation of Amygdala Function. *Neuron* **48**, 1025–1037 (2005).
- 551 92. Naylor, J. C. *et al.* Dopamine attenuates evoked inhibitory synaptic currents in central amygdala neurons.
552 *Eur. J. Neurosci.* **32**, 1836–1842 (2010).

- 553 93. Rosenkranz, J. A. & Grace, A. A. Modulation of basolateral amygdala neuronal firing and afferent drive by
554 dopamine receptor activation in vivo. *J. Neurosci. Off. J. Soc. Neurosci.* **19**, 11027–11039 (1999).
- 555 94. Rosenkranz, J. A. & Grace, A. A. Cellular mechanisms of infralimbic and prelimbic prefrontal cortical
556 inhibition and dopaminergic modulation of basolateral amygdala neurons in vivo. *J. Neurosci. Off. J. Soc.*
557 *Neurosci.* **22**, 324–337 (2002).
- 558 95. Silberman, Y. & Winder, D. G. Corticotropin releasing factor and catecholamines enhance glutamatergic
559 neurotransmission in the lateral subdivision of the central amygdala. *Neuropharmacology* **70**, 316–323
560 (2013).
- 561 96. Beckstead, M. J., Grandy, D. K., Wickman, K. & Williams, J. T. Vesicular dopamine release elicits an
562 inhibitory postsynaptic current in midbrain dopamine neurons. *Neuron* **42**, 939–946 (2004).
- 563 97. Marcott, P. F. *et al.* Regional heterogeneity of D2-receptor signaling in the dorsal striatum and nucleus
564 accumbens. *Neuron* **98**, 575-587.e4 (2018).
- 565 98. Bettler, B., Kaupmann, K., Mosbacher, J. & Gassmann, M. Molecular structure and physiological functions
566 of GABA(B) receptors. *Physiol. Rev.* **84**, 835–867 (2004).
- 567 99. Destexhe, A. & Sejnowski, T. J. G protein activation kinetics and spillover of gamma-aminobutyric acid
568 may account for differences between inhibitory responses in the hippocampus and thalamus. *Proc. Natl.*
569 *Acad. Sci. U. S. A.* **92**, 9515–9519 (1995).
- 570 100. Mackay, J. P. *et al.* NPY2 Receptors Reduce Tonic Action Potential-Independent GABAB Currents in the
571 Basolateral Amygdala. *J. Neurosci.* **39**, 4909–4930 (2019).
- 572 101. Cauli, B. *et al.* Classification of fusiform neocortical interneurons based on unsupervised clustering. *Proc.*
573 *Natl. Acad. Sci. U. S. A.* **97**, 6144–6149 (2000).
- 574 102. Guthman, E. M. *et al.* Cell-type-specific control of basolateral amygdala neuronal circuits via entorhinal
575 cortex-driven feedforward inhibition. *eLife* <https://elifesciences.org/articles/50601/figures> (2020)
576 doi:10.7554/eLife.50601.

- 577 103. Hou, W.-H. *et al.* Wiring Specificity and Synaptic Diversity in the Mouse Lateral Central Amygdala. *J.*
578 *Neurosci. Off. J. Soc. Neurosci.* **36**, 4549–4563 (2016).
- 579 104. Chieng, B. C. H., Christie, M. J. & Osborne, P. B. Characterization of neurons in the rat central nucleus of
580 the amygdala: cellular physiology, morphology, and opioid sensitivity. *J. Comp. Neurol.* **497**, 910–927
581 (2006).
- 582 105. Dumont, E. C., Martina, M., Samson, R. D., Drolet, G. & Paré, D. Physiological properties of central
583 amygdala neurons: species differences. *Eur. J. Neurosci.* **15**, 545–552 (2002).
- 584 106. Lopez de Armentia, M. & Sah, P. Firing properties and connectivity of neurons in the rat lateral central
585 nucleus of the amygdala. *J. Neurophysiol.* **92**, 1285–1294 (2004).
- 586 107. Fadok, J. P., Markovic, M., Tovote, P. & Lüthi, A. New perspectives on central amygdala function. *Curr.*
587 *Opin. Neurobiol.* **49**, 141–147 (2018).
- 588 108. Gungor, N. Z. & Paré, D. Functional Heterogeneity in the Bed Nucleus of the Stria Terminalis. *J. Neurosci.*
589 **36**, 8038–8049 (2016).
- 590 109. Tovote, P. *et al.* Midbrain circuits for defensive behaviour. *Nature* **534**, 206–212 (2016).
- 591 110. Padilla, S. L. *et al.* AgRP Neural Circuits Mediate Adaptive Behaviors in the Starved State. *Nat. Neurosci.*
592 **19**, 734–741 (2016).
- 593 111. Gullledge, A. T. & Jaffe, D. B. Multiple effects of dopamine on layer V pyramidal cell excitability in rat
594 prefrontal cortex. *J. Neurophysiol.* **86**, 586–595 (2001).
- 595 112. Vander Weele, C. M. *et al.* Dopamine enhances signal-to-noise ratio in cortical-brainstem encoding of
596 aversive stimuli. *Nature* **563**, 397 (2018).
- 597 113. White, C. M., Ji, S., Cai, H., Maudsley, S. & Martin, B. Therapeutic potential of vasoactive intestinal
598 peptide and its receptors in neurological disorders. *CNS Neurol. Disord. Drug Targets* **9**, 661 (2010).
- 599 114. Nagata-Kuroiwa, R. *et al.* Critical Role of Neuropeptides B/W Receptor 1 Signaling in Social Behavior and
600 Fear Memory. *PLoS ONE* **6**, (2011).

- 601 115. Tanaka, H. *et al.* Characterization of a family of endogenous neuropeptide ligands for the G protein-
602 coupled receptors GPR7 and GPR8. *Proc. Natl. Acad. Sci.* **100**, 6251–6256 (2003).
- 603 116. Chen, Y. *et al.* Sustained NPY signaling enables AgRP neurons to drive feeding. *eLife* **8**, (2019).
- 604 117. Watanabe, N. *et al.* A single nucleotide polymorphism of the neuropeptide B/W receptor-1 gene
605 influences the evaluation of facial expressions. *PLoS One* **7**, e35390 (2012).
- 606 118. Kingsbury, M. A. & Wilson, L. C. The Role of VIP in Social Behavior: Neural Hotspots for the Modulation of
607 Affiliation, Aggression, and Parental Care. *Integr. Comp. Biol.* **56**, 1238–1249 (2016).
- 608 119. Reiner, A. *et al.* Revised nomenclature for avian telencephalon and some related brainstem nuclei. *J.*
609 *Comp. Neurol.* **473**, 377–414 (2004).
- 610 120. Wilson, L. C., Goodson, J. L. & Kingsbury, M. A. Seasonal Variation in Group Size Is Related to Seasonal
611 Variation in Neuropeptide Receptor Density. *Brain. Behav. Evol.* **88**, 111–126 (2016).
- 612 121. Schindelin, J. *et al.* Fiji: an open-source platform for biological-image analysis. *Nat. Methods* **9**, 676–682
613 (2012).
- 614 122. McQuin, C. *et al.* CellProfiler 3.0: Next-generation image processing for biology. *PLoS Biol.* **16**, e2005970
615 (2018).
- 616 123. Paxinos, G. & Franklin, K. B. J. *The mouse brain in stereotaxic coordinates.* (Academic, 2004).
- 617 124. Paxinos, G. & Franklin, K. B. J. *Paxinos and Franklin's The mouse brain in stereotaxic coordinates.*
618 (Academic Press, an imprint of Elsevier, 2019).
- 619 125. Bogovic, J. A., Hanslovsky, P., Wong, A. & Saalfeld, S. Robust Registration of Calcium Images by Learned
620 Contrast Synthesis. *2016 IEEE 13th Int. Symp. Biomed. Imaging ISBI* 1123–1126 (2016)
621 doi:10.1109/ISBI.2016.7493463.
- 622 126. Conte, W. L., Kamishina, H. & Reep, R. L. Multiple neuroanatomical tract-tracing using fluorescent Alexa
623 Fluor conjugates of cholera toxin subunit B in rats. *Nat. Protoc.* **4**, 1157–1166 (2009).
- 624 127. Hunter, J. D. Matplotlib: A 2D Graphics Environment. *Comput. Sci. Eng.* **9**, 90–95 (2007).
- 625 128. Pedregosa, F. *et al.* Scikit-learn: Machine Learning in Python. *J. Mach. Learn. Res.* **12**, 2825–2830 (2011).

- 626 129. Gottman, J. M. & Roy, A. K. *Sequential Analysis: A Guide for Behavioral Researchers*. (Cambridge
627 University Press, 1990).
- 628 130. Novák, P. & Zahradník, I. Q-Method for High-Resolution, Whole-Cell Patch-Clamp Impedance
629 Measurements Using Square Wave Stimulation. *Ann. Biomed. Eng.* **34**, 1201–1212 (2006).
- 630 131. Virtanen, P. *et al.* SciPy 1.0: fundamental algorithms for scientific computing in Python. *Nat. Methods* **17**,
631 261–272 (2020).
- 632 132. Ward, J. H. Hierarchical Grouping to Optimize an Objective Function. *J. Am. Stat. Assoc.* **58**, 236–244
633 (1963).
- 634 133. Michael Waskom *et al.* *mwaskom/seaborn: v0.11.0 (September 2020)*. (Zenodo, 2020).
635 doi:10.5281/zenodo.4019146.
- 636

637 **Figure Legends**

638 **Fig. 1. DRN^{DAT}-CeA photostimulation promotes sociability but DRN^{DAT}-BLP mediates place**
639 **avoidance. a**, AAV₅-DIO-ChR2-eYFP or AAV₅-DIO-eYFP was injected into the DRN of DAT::Cre mice
640 and optic fibers implanted over the BNST, CeA, or BLP to photostimulate DRN^{DAT} terminals. After >7
641 weeks to allow for viral expression, cages of mice were assayed for social dominance using the tube
642 test, prior to other behavioral tasks. **b**, Heatmaps showing the relative location of ChR2-expressing mice
643 in the three-chamber sociability assay, with optic fibers located over the BNST (left), CeA (center), or
644 BLP (right). The task was repeated across two days, with one session paired with photostimulation
645 ('ON') and one without ('OFF'). **c**, Photostimulation of DRN^{DAT}-CeA terminals (8 pulses of 5 ms pulse-
646 width 473 nm light, delivered at 30 Hz every 5 s) in ChR2-expressing mice (ChR2^{CeA}) increased time
647 spent in the social zone relative to the object zone ('social:object ratio'; paired t-test: $t_{28}=2.91$; corrected
648 for multiple comparisons across projections: $p=0.021$; $n=29$), but had no significant effect on ChR2^{BNST}
649 mice (paired t-test: $t_{26}=0.552$, $p=0.586$; $n=27$), ChR2^{BLP} mice (paired t-test: $t_{13}=1.62$, $p=0.13$, $n=14$), nor
650 eYFP mice. **d**, Scatter plots displaying relative dominance plotted against the change in social zone
651 time with optical stimulation (ON-OFF), showing significant positive correlation in ChR2^{CeA} mice
652 (Pearson's correlation: $r=0.549$, $p=0.002$). Inset bar graphs show mean values for subordinate,
653 intermediate, and dominant mice. **e**, Example tracks of ChR2^{BNST}, ChR2^{CeA}, and ChR2^{BLP} mice in the
654 real-time place preference (RTPP) assay, and bar graphs showing the difference in % time spent in the
655 stimulated ('ON') and unstimulated ('OFF') zones. ChR2^{BLP} mice spent proportionally less time in the
656 stimulated zone relative to eYFP^{BLP} mice (unpaired t-test: $t_{13}=2.13$, $p=0.0455$, $n=14$ ChR2^{BLP}, $n=8$
657 eYFP^{BLP}). **f**, Time spent in the ON zone across the 30 min session. ChR2^{BLP} mice spent significantly
658 less time in the ON zone relative to eYFP^{BLP} mice at 15 min (repeated measures two-way ANOVA: $F_{1,20}$
659 $= 4.53$, main effect of opsin $p=0.046$, Bonferroni post-hoc tests $*p<0.05$ at 15 min). **g**, Scatter plots
660 showing relative dominance plotted against the difference in zone time (insets show mean values for
661 subordinate, intermediate, and dominant mice). Bar and line graphs display mean \pm SEM. $*p<0.05$,
662 $**p<0.01$.

663 **Fig. 2. Collateralization of DRN^{DAT} projections. a**, The retrograde tracer cholera toxin subunit-B (CTB)
664 conjugated to Alexa Fluor 555 (CTB-555, magenta) or Alexa-Fluor 647 (CTB-647, cyan) was injected
665 into two downstream targets. **b**, Confocal images showing representative injection sites for dual BNST
666 and CeA injections (left panels), BNST and BLP (center panels), and CeA and BLP (right panels). **c**,
667 High magnification images of DRN cells expressing CTB-555 (magenta), CTB-647 (cyan), and TH
668 (green) following injection into the BNST and CeA. White arrows indicate triple-labelled cells. **d**, Venn
669 diagrams showing the proportion of CTB+/TH+ cells in the DRN following dual injections placed in the
670 BNST and CeA (left), BNST and BLP (center), or CeA and BLP (right). When injections were placed in
671 the BNST and CeA, dual CTB-labelled TH+ cells constituted 46% of all BNST projectors and 55% of all
672 CeA projectors. In contrast, when injections were placed in the BNST and BLP, or CeA and BLP, the
673 proportion of dual-labelled cells was considerably lower (7.6% of BNST projectors and 9.7% of CeA
674 projectors). **e**, Heatmaps indicating the relative density of TH+ CTB+ cells throughout the DRN/CLi for
675 each projector population and **f**, dual-labelled cells. Color intensity represents average number of cells
676 per slice. The total number of TH+ BNST and CeA projectors per slice was similar ($n=27.9$ BNST
677 projectors and $n=27.2$ CeA projectors per slice), whereas TH+ BLP projectors were significantly fewer
678 in number ($n=6.4$ BLP projectors per slice; Kruskal-Wallis statistic = 83.5, $p<0.0001$; Dunn's post-hoc
679 tests: BNST vs. CeA $p>0.05$, BNST vs BLP $p<0.001$, CeA vs BLP $p<0.001$). TH+ BNST and CeA
680 projectors, and dual-labelled cells, were broadly distributed throughout the DRN, vIPAG, and CLi, with

681 a higher concentration in the dorsal aspect of the DRN, whereas BLP projectors tended to be relatively
682 denser in ventral DRN/CLi.

683

684 **Fig. 3. Spatial-segregation of dopamine and neuropeptide receptor populations within DRN^{DAT}**
685 **terminal fields. a**, Average image showing terminal density in the middle anteroposterior (AP) region
686 of the BNST, following eYFP expression in DRN^{DAT} (left) or VTA^{DAT} (right) neurons. **b**, Average images
687 showing fluorescent puncta in the BNST indicating detection of *Drd1* (red), *Drd2* (yellow), *Vipr2* (green),
688 or *Npbwr1* (blue) mRNA transcripts. **c**, Line graphs showing the percent of cells expressing each
689 receptor (≥ 5 puncta) across AP locations for the oval nucleus, dorsolateral BNST, and dorsomedial
690 BNST (two-way ANOVA, oval nucleus: RNA probe x AP interaction, $F_{9,160}=6.194$, $p<0.0001$,
691 dorsolateral BNST: RNA probe x AP interaction, $F_{12,167}=3.410$, $p=0.0002$, dorsomedial BNST: RNA
692 probe x AP interaction, $F_{12,161}=2.268$, $p=0.0110$). *Drd1*: $n=51,55,53$, *Drd2*: $n=52,55,53$, *Vipr2*:
693 $n=37,39,37$, *Npbwr1*: $n=36,38,38$ sections, for oval nucleus, dorsolateral BNST, and dorsomedial
694 BNST, respectively, from 4 mice. **d**, Matrices indicating overlap between mRNA-expressing cells:
695 square color indicates the percent of cells expressing the gene in the column from within cells
696 expressing the gene in the row. **e**, Average image showing terminal density in the middle AP region of
697 the CeA, following eYFP expression in DRN^{DAT} (left) or VTA^{DAT} (right) neurons. **f**, Average images
698 showing fluorescent puncta in the CeA indicating mRNA expression. **g**, Line graphs showing the % of
699 cells expressing each receptor (≥ 5 puncta) across AP locations for the CeL, CeM, and CeC (two-way
700 ANOVA, CeL: RNA probe x AP interaction, $F_{12,220}=8.664$, $p<0.0001$, CeM: main effect of RNA probe,
701 $F_{3,186}=60.30$, $p<0.0001$, CeC: RNA probe x AP interaction, $F_{12,218}=4.883$, $p<0.0001$). *Drd1*: $n=47,40,47$,
702 *Drd2*: $n=70,55,70$, *Vipr2*: $n=65,57,63$, *Npbwr1*: $n=62,50,60$ sections, for CeL, CeM, and CeC,
703 respectively, from 4 mice. **h**, Matrices indicating overlap between mRNA-expressing cells. **i**, Average
704 image showing terminal density in the middle AP region of the BLP, following eYFP expression in
705 DRN^{DAT} (left) or VTA^{DAT} (right) neurons. **j**, Average images showing fluorescent puncta in the BLP
706 indicating mRNA expression. **k**, Line graphs showing the percent of cells expressing each receptor (≥ 5
707 puncta) across AP locations for the BLP and BMP (two-way ANOVA, BLP: RNA probe x AP interaction,
708 $F_{15,176}=2.165$, $p=0.0091$, BMP: main effect of RNA probe, $F_{3,141}=56.92$, $p<0.0001$). *Drd1*: $n=55,44$ *Drd2*:
709 $n=59,46$ *Vipr2*: $n=41,33$ *Npbwr1*: $n=45,34$ sections, for BLP and BMP, respectively, from 4 mice. **l**,
710 Matrices indicating overlap between mRNA-expressing cells. Line graphs show mean \pm SEM.

711 **Fig. 4. DRN^{DAT} input influences downstream activity in a cell type-dependent manner. a**, In mice
712 expressing ChR2 in DRN^{DAT} neurons, *ex vivo* electrophysiological recordings were made from the
713 BNST, **b**, CeA, and **c**, BLP. **d**, Photostimulation of DRN^{DAT} terminals with blue light (8 pulses delivered
714 at 30 Hz) evoked both excitatory and inhibitory responses at resting membrane potentials in the BNST,
715 **e**, CeA, and **f**, BLP. Traces show single sweeps and pie charts indicate proportion of cells with no
716 response ('none'), an EPSP only ('excitation'), an IPSP only ('inhibition'), or a mixed response ('mix').
717 Recorded cells: BNST $n=19$, CeA $n=36$, BLP $n=48$, from 19 mice. **g**, When constant current was injected
718 to elicit spontaneous firing, BNST cells responded to photostimulation with an increase in firing
719 ('excitation'), while **h**, CeA and **i**, BLP cells responded with an increase or a decrease in firing
720 ('inhibition'). Recorded cells: BNST $n=5$, CeA $n=20$, BLP $n=17$. **j**, Properties of the optically-evoked
721 excitatory post-synaptic potential (EPSP) at resting membrane potentials – left: peak amplitude
722 (Kruskal-Wallis statistic = 6.790, $p=0.0335$; Dunn's posts-hoc tests: CeA vs BLP $p=0.0378$); middle:
723 change in amplitude across light pulses; right: violin plots showing distribution of onset latencies (white
724 circle indicates median). **k**, Properties of the optically-evoked inhibitory post-synaptic potential (EPSP)

725 at resting membrane potentials – left: trough amplitude (one-way ANOVA, $F_{2,31}=8.150$, $p=0.0014$, CeA
726 vs BLP: $**p=0.0014$); middle: violin plot showing latency to trough peak; right: violin plot showing tau for
727 the current decay (white circle indicates median). Bar and line graphs display mean \pm SEM. $*p<0.05$,
728 $**p<0.01$. **l**, Workflow for agglomerative hierarchical clustering of CeA neurons and **m**, BLP neurons.
729 Four baseline electrical properties were used as input features, following max-min normalization (see
730 *Methods*) and Ward's method used to generate a cluster dendrogram, grouping cells based on
731 Euclidean distance. **n**, Dendrogram for CeA cells indicating two major clusters, with their response to
732 DRN^{DAT} input indicated below each branch (excitation=black; inhibition=grey; no response=open). **o**,
733 Upper panels: cluster 1 showed baseline properties typical of 'late-firing' neurons and cluster 2 showed
734 baseline properties typical of 'regular-firing' neurons. Lower panels: pie charts showing the response of
735 cells in each cluster to DRN^{DAT} input. **p**, Dendrogram for BLP cells indicating two major clusters, with
736 their response to DRN^{DAT} input indicated below each branch (excitation=black; inhibition=grey; no
737 response=open). **q**, Upper panels: cluster 1 showed baseline properties typical of pyramidal neurons
738 and cluster 2 showed baseline properties typical of GABA interneurons. Lower panels: pie charts
739 showing the response of cells in each cluster to DRN^{DAT} input.

740

741 **Supplementary Figure Legends**

742 **Fig. S1. DRN^{DAT} and VTA^{DAT} afferents target distinct downstream regions. Related to Fig. 1 and**
743 **Fig. 3. a-d**, Confocal images at different AP locations through the VTA and DRN showing the typical
744 spread of eYFP expression (green) following an injection of AAV₅-DIO-ChR2-eYFP into **a-b**, the DRN
745 and **c-d**, the VTA. Tyrosine hydroxylase (TH; the rate limiting enzyme in dopamine synthesis)
746 expression from immunohistochemistry is shown in red. **b,d**, High magnification images of the
747 substantia nigra pars compacta (SNc), VTA, rostral linear nucleus (RLi), caudal linear nucleus (CLi),
748 and DRN. Viral injection in the DRN typically resulted in eYFP-expressing cells within the DRN,
749 ventrolateral periaqueductal grey (vIPAG), and CLi nuclei, with minimal expression in the RLi, and none
750 in the VTA or substantia nigra pars compacta (SNc). In contrast, viral injection in the VTA produced
751 robust eYFP expression in SNc and VTA cell bodies, with some RLi expression, and none in the CLi,
752 vIPAG, or DRN. **e**, Example images of downstream regions showing TH expression from
753 immunohistochemistry and **f**, eYFP expression in the prefrontal cortex (PFC), nucleus accumbens
754 (NAc), bed nucleus of the stria terminalis (BNST), central amygdala (CeA), and posterior basolateral
755 amygdala (BLP) following injection into the DRN (upper panels) and the VTA (lower panels). **g**,
756 Quantification of mean eYFP fluorescence in subregions from each structure (PFC: n=18 and 14
757 sections, striatum: n=20 and 21 sections, BNST: n=14 and 13 sections, CeA: n=24 and 27 sections,
758 amygdala: n=45 and 51 sections from DRN and VTA injections, respectively, from 6 mice). eYFP
759 fluorescence was significantly greater following VTA injection in all striatal subregions (unpaired t-test:
760 CPu: $t_{39}=13.23$, $p<0.0001$; NAc core: $t_{39}=13.56$, $p<0.0001$; NAc lateral shell: $t_{31}=13.01$, $p<0.0001$; NAc
761 medial shell: $t_{37}=4.49$, $p<0.0001$), and significantly greater following DRN injection in the BNST oval
762 nucleus (unpaired t-test: $t_{22}=3.95$, $p=0.0007$) and CeA lateral division (unpaired t-test: unpaired t-test:
763 $t_{34}=3.18$, $p=0.0031$). **h**, Images from three selected downstream targets showing average terminal
764 density in the middle anteroposterior (AP) region following eYFP expression in DRN^{DAT} (left) or VTA^{DAT}
765 (right) neurons. Bar graphs show mean \pm SEM. PFC: Cg=cingulate cortex, PL=prelimbic cortex, IL=
766 infralimbic cortex; striatum: CPu=caudate putamen, NAc core=nucleus accumbens core, NAc
767 l.sh.=nucleus accumbens lateral shell, NAc m.sh.=nucleus accumbens medial shell; BNST: oval nuc.=
768 BNST oval nucleus, lat.=BNST lateral division, med.=BNST medial division, vent.=BNST ventral part;
769 CeL=central amygdala lateral division, CeM, central amygdala medial division, CeC=central amygdala
770 capsular division; amygdala: LA=lateral amygdala, BLA=basolateral amygdala, BLP=basolateral
771 amygdala posterior.

772 **Fig. S2. Analysis of baseline behavioral traits and state transition in the juvenile intruder task.**
773 **Related to Fig 1. a**, Example confocal images showing ChR2-expressing DRN^{DAT} terminals and fiber
774 placement over the BNST, **b**, CeA, and **c**, BLP. **d**, The tube test for social dominance was performed
775 prior to optogenetic manipulations. **e**, Proportion of wins for an individual cage tested across four days,
776 and average for all cages used in optogenetic manipulation experiments, separated by number of mice
777 per cage (red=dominant, orange=intermediate, yellow=subordinate). **f**, Correlation matrix indicating the
778 relationship between baseline behavioral measures for all mice used in Fig. 1 and Fig. S3. For the open
779 field test (OFT) and elevated-plus maze (EPM) the first 5 min of the task were used and for the juvenile
780 intruder and 3 chamber assays the data from the 'OFF' session was used. **g**, Principal component
781 analysis (PCA) of behavioral measures with point color representing the social dominance score for
782 each animal. Inset, scree plot showing % variance explained by the first 5 PCs. **h-i**, Home-cage behavior
783 was assessed in the juvenile intruder assay across two counterbalanced sessions, one paired with
784 photostimulation ('ON') and one without ('OFF'). DRN^{DAT}-CeA photostimulation in ChR2-expressing

785 mice increased time spent engaged in face investigation with the juvenile mouse (paired t-test: $t_{22}=2.36$,
786 $p = 0.027$), whereas **j-k**, DRN^{DAT}-BNST photostimulation increased time spent rearing (paired t-test:
787 $t_{23}=2.32$, $p=0.0298$). **l**, A two-state Markov model was used to examine behavioral transitions during the
788 juvenile intruder assay for DRN^{DAT}-CeA mice. **m**, Bar graphs showing the difference in transition
789 probability (ON-OFF) for within-state transitions and across-state transitions, for ChR2^{CeA} and ChR2^{eYFP}
790 mice. There was no significant difference between ChR2 and eYFP groups for the change in within-
791 state transition probability (two-way ANOVA: opsin x transition interaction, $F_{1,37}=3.149$, $p=0.0842$) or
792 across-state transition probability (two-way ANOVA: opsin x transition interaction, $F_{1,37}=0.542$, $p=0.466$)
793 with photostimulation. Graphs show mean \pm SEM.

794

795 **Fig. S3. Photostimulation of DRN^{DAT} projections does not modify locomotor or anxiety-like**
796 **behavior, or support self-stimulation. Related to Fig 1. a**, Example tracks in the open field test from
797 a ChR2^{BNST}, **b**, ChR2^{CeA}, and **c**, ChR2^{BLP} mouse. Photostimulation had no significant effect on time
798 spent in the center of the open field (two-way ANOVA, light x group interaction, BNST – $F_{2,94}=0.105$,
799 $p=0.901$; CeA – $F_{2,98}=0.613$, $p=0.544$; BLP – $F_{2,40}=0.181$, $p=0.835$) or distance travelled (two-way
800 ANOVA, light x group interaction, BNST – $F_{2,94}=0.157$, $p=0.855$; CeA – $F_{2,98}=0.163$, $p=0.850$; BLP –
801 $F_{2,40}=0.252$, $p=0.771$) for DRN^{DAT}-BNST, DRN^{DAT}-CeA, or DRN^{DAT}-BLP mice. **d**, Example tracks in the
802 elevated plus maze (EPM) from a ChR2^{BNST}, **e**, ChR2^{CeA}, and **f**, ChR2^{BLP} mouse. Photostimulation had
803 no significant effect on time spent in the open arms of the EPM (two-way ANOVA, light x group
804 interaction, BNST – $F_{2,58}=0.896$, $p=0.414$, CeA – $F_{2,78}=0.160$, $p=0.852$, BLP – $F_{2,40}=0.354$, $p=0.704$) for
805 DRN^{DAT}-BNST, DRN^{DAT}-CeA, or DRN^{DAT}-BLP mice. **g-i**, Photostimulation of the DRN^{DAT}-BNST,
806 DRN^{DAT}-CeA, or DRN^{DAT}-BLP projection did not support intra-cranial self-stimulation (ICSS) as shown
807 by a lack of preference for the active nosepoke (paired with blue light delivery) over the inactive
808 nosepoke. **j**, Scatter plots displaying the change in face investigation against the change in rearing with
809 photostimulation (ON-OFF) for ChR2^{BNST}, **k**, ChR2^{CeA}, **l**, and ChR2^{BLP} mice in the juvenile intruder
810 assay. Outer plots are probability density curves, using kernel density estimation, to show the
811 distribution of each behavior. Line and bar graphs show mean \pm SEM.

812

813 **Fig. S4. Verification of dual-retrograde tracing strategy and intersectional approach to reveal**
814 **axon collaterals. Related to Fig 2. a**, Two retrograde tracers (CTB-555 and CTB-647) were injected
815 into the same location, followed by sectioning and immunohistochemistry after 7 days. Right panels
816 show example injection site for CTB-555 and CTB-647 in the BNST. **b**, CTB-expressing cells in the
817 DRN with TH (green) revealed by immunohistochemistry. White arrows indicate triple-labelled cells. **c**,
818 Within the TH+ cells in the DRN, injection of both retrograde tracers into the same location resulted in
819 97% CTB-647+ cells co-labelled with CTB-555, and 100% CTB-555+ cells co-labelled with CTB-647.
820 **d**, Injection strategy to enable eYFP expression selectively in the DRN^{DAT}-CeA projection. A
821 retrogradely-travelling HSV construct encoding mCherry-flpo, expressed in a Cre-dependent manner
822 (HSV-LS1L-mCherry-IRES-flpo), was injected into the CeA of a DAT::Cre mouse, and an AAV,
823 expressed in a flpo-dependent manner, encoding eYFP (AAV₅-fDIO-eYFP) was injected into the DRN.
824 **e**, After 7 weeks, this resulted in eYFP-expressing TH+ cells in the DRN, and **f**, eYFP-expressing
825 processes in both the CeA (upper panels) and BNST (lower panels). **g**, Injection of only AAV₅-fDIO-
826 eYFP into the DRN of a DAT::Cre mouse did not result in eYFP expression.

827 **Fig. S5. Analysis of mRNA expression using different thresholds. Related to Fig 3.** **a**, Workflow
828 for RNAscope and image processing. **b**, Scatter plots showing a linear relationship between fluorescent
829 pixels/cell and number of puncta/cell for three separate sections for each probe. **c**, Violin plots displaying
830 puncta count per section for each receptor in the BNST (white circle indicates median; *Drd1*: n=51,55,53
831 *Drd2*: n=52,55,53 *Vipr2*: n=37,39,37 *Npbwr1*: n=36,38,38 sections, for oval nucleus, dorsolateral BNST,
832 and dorsomedial BNST, respectively, from 4 mice). **d**, Line graphs for each BNST subregion showing
833 the number of expressing cells when using a threshold of 1 punctum/cell and **e**, 3 puncta per cell. **f**,
834 Violin plots displaying puncta count per section for each receptor in the CeA (white circle indicates
835 median; *Drd1*: n=47,40,47 *Drd2*: n=70,55,70 *Vipr2*: n=65,57,63 *Npbwr1*: n=62,50,60 sections, for CeL,
836 CeM, and CeC, respectively, from 4 mice). **g**, Line graphs for each CeA subregion showing the number
837 of expressing cells when using a threshold of 1 punctum/cell and **h**, 3 puncta per cell. **i**, Violin plots
838 displaying puncta count per section for each receptor in the amygdala (white circle indicates median;
839 *Drd1*: n=55,44 *Drd2*: n=59,46 *Vipr2*: n=41,33 *Npbwr1*: n=45,34 sections, for BLP and BMP,
840 respectively, from 4 mice). **j**, Line graphs for each amygdala subregion showing the number of
841 expressing cells when using a threshold of 1 punctum/cell and **k**, 3 puncta per cell. These lower
842 thresholds yielded more expressing cells than using 5 puncta/cell (compare with Fig. 3c,g,k), but with a
843 similar expression pattern across subregions and AP location. **l-m**, Example images showing
844 expression of *Vipr1* and *Vipr2* within the BNST and CeA. We typically observed greater *Vipr2* than *Vipr1*
845 expression, and high co-localization, and therefore concentrated our detailed analyses on *Vipr2*. Line
846 graphs show mean±SEM.

847

848 **Fig. S6. Effect of DRN^{DAT} photostimulation on downstream cellular excitability ex vivo. Related**
849 **to Fig 4.** **a**, Example DIC image, and corresponding eYFP fluorescence, of a brain slice containing the
850 BNST, **b**, CeA, or **c**, BLP during *ex vivo* recording. Regional maps show the location of recorded cells,
851 with color indicating the change in membrane potential elicited by optical stimulation of DRN^{DAT}
852 terminals. **d**, Example traces showing the optically-evoked EPSP (upper panels) and slow component
853 of the IPSP (lower panels) was maintained following application of TTX/4AP. **e**, Normalized peak
854 amplitude of the EPSP and IPSP following TTX/4AP (EPSP, n=8; IPSP, n=3). **f**, Scatter plots showing
855 the amplitude of the optically-evoked EPSP (left) and IPSP (right) recorded in downstream locations
856 plotted against baseline membrane potential. **g**, Line graphs showing the action potential inter-event
857 interval (IEI) in cells where constant current was injected to elicit firing. Raw (left) and normalized (right)
858 IEI 5.5 s before and 5 s after optical stimulation of DRN^{DAT} terminals (blue shading) in BNST, CeA, and
859 BLP cells. Cells which showed a reduction in IEI with optical stimulation were labelled 'excited' (excit.,
860 black) and cells which showed an increase in IEI with optical stimulation were defined as 'inhibited'
861 (inhib., grey). **h**, Box-and-whisker plots comparing the baseline cell properties (used as input features
862 for hierarchical clustering; Fig. 4l-q) of the two CeA clusters and **i**, the two BLP clusters. Unpaired t-
863 tests for CeA – ramp ratio: $t_{24}=3.502$, $p=0.0018$; max instantaneous firing frequency (max freq_{inst.}):
864 $t_{24}=4.698$, $p<0.0001$, firing delay: $t_{24}=5.050$, $p<0.0001$, voltage sag: $t_{24}=3.983$, $p=0.0006$; unpaired t-
865 tests for BLP – capacitance: $t_{25}=4.803$, $p<0.0001$, max freq_{inst.}: $t_{25}=15.48$, $p<0.0001$, firing delay:
866 $t_{25}=2.743$, $p=0.0111$, voltage sag: $t_{25}=2.705$, $p=0.0121$. **j**, Box-and-whisker plots for the two CeA clusters
867 and **k**, the two BLP clusters showing the amplitude and latency of the EPSP and IPSP, and the
868 combined total voltage area elicited by optical stimulation of DRN^{DAT} terminals. EPSP peak amplitude,
869 CeA: unpaired t-test, $t_{17}=1.40$, $p=0.180$; BLP: unpaired t-test $t_{22}=2.34$, $p=0.029$. EPSP latency, CeA:
870 unpaired t-test, $t_{17}=0.673$, $p=0.510$; BLP: Mann-Whitney $U = 33.5$, $p=0.032$. Total voltage area, CeA:

871 Mann-Whitney $U = 22$, $p=0.0023$; BLP: Mann-Whitney $U = 29$, $p=0.0019$. **i**, Workflow for agglomerative
872 hierarchical clustering of all CeA and BLP neurons combined. Five cell properties were used as input
873 features, corresponding to the five used in Fig. 4l-q for separate clustering of CeA and BLP cells. **m**,
874 Dendrogram indicating two major clusters, with the cell location and response to DRN^{DAT} input indicated
875 by the colored bars below each branch (CeA – pink, BLP – blue; excitation=black; inhibition=grey; no
876 response=open). **n**, Pie charts showing the response of cluster 1 and cluster 2 CeA cells (upper) and
877 BLP cells (lower) to optical stimulation DRN^{DAT} input. * $p<0.05$, ** $p<0.01$, *** $p<0.001$, **** $p<0.0001$.

878

879

880

881 **Methods**

882 ***Animals and housing***

883 All procedures involving animals were conducted in accordance with NIH guidelines and
884 approved by the MIT Committee on Animal Care or the Salk Institute Institutional Animal Care and Use
885 Committee. DAT::IRES-Cre (B6.SJL-Slc6a3^{tm1.1(cre)Bkmn/J})³⁵ were purchased from the Jackson
886 Laboratory (stock no. 006660; the Jackson Laboratory, ME, USA) and bred in-house to generate
887 heterozygous male offspring for experiments. Wild-type C57BL/6J mice were purchased from Charles
888 River Laboratories (MA, USA). Mice were housed on a 12h:12h reverse light dark cycle (MIT: lights off
889 9am-9pm; Salk Institute: lights off 9.30am-9.30pm) with food and water available *ad libitum*. Mice were
890 housed in groups of 2-4 with same-sex siblings.

891 ***Surgery and viral constructs***

892 Mice (>7 weeks of age) were anaesthetized with isoflurane (inhalation: 4% for induction, ~2%
893 for maintenance, oxygen flow rate 1 L/min) before being placed in a digital small animal stereotax (David
894 Kopf Instruments, CA, USA). Surgeries were performed under aseptic conditions with body temperature
895 maintained by a heating pad throughout. Injections of recombinant adeno-associated viral (AAV)
896 vectors, herpes simplex virus (HSV), or cholera toxin subunit-B (CTB) were performed using a beveled
897 33 gauge microinjection needle with a 10 µL microsyringe (Nanofil; WPI, FL, USA). Virus or CTB was
898 delivered at a rate of 0.1 µL/min using a microsyringe pump (UMP3; WPI, FL, USA) connected to a
899 Micro4 controller (WPI, FL, USA). Following injection, the needle was maintained in place for ~2 min,
900 then raised up by 0.05 mm and held for ~10 min (to permit diffusion from the injection site) before being
901 slowly withdrawn. Skull measurements were made relative to Bregma for all injections and implants.
902 Implants were secured to the skull by a layer of adhesive cement (C&B Metabond; Parkell Inc., NY,
903 USA) followed by a layer of black cranioplastic cement (Ortho-Jet; Lang, IL, USA). Mice were given pre-
904 emptive analgesia (1 mg/kg buprenorphine slow-release; sub-cutaneous; delivered concurrent with
905 warmed Ringer's solution to prevent dehydration), supplemented with meloxicam (1.5 mg/kg; sub-
906 cutaneous) where necessary, and were monitored on a heating pad until recovery from anesthesia.

907 AAV₅-EF1α-DIO-ChR2-eYFP, AAV₅-EF1α-DIO-eYFP, and AAV₅-EF1α-fDIO-eYFP were
908 packaged by the University of North Carolina Vector Core (NC, USA) and received the AAV₅-EF1α-
909 fDIO-eYFP construct from Karl Deisseroth and Charu Ramakrishnan. HSV-LS1L-mCherry-IRES-flpo
910 was packaged by Dr. Rachael Neve at the Viral Gene Transfer Core Facility at MIT (now located at
911 Massachusetts General Hospital).

912 ***Immunohistochemistry and confocal microscopy***

913 Mice were deeply anaesthetized with sodium pentobarbital (200 mg/kg, intraperitoneal; IP) or
914 euthasol (150 mg/kg; IP) followed by transcardial perfusion with 10 mL ice-cold Ringer's solution and
915 15 mL ice-cold 4% paraformaldehyde (PFA). The brain was carefully dissected from the cranial cavity
916 and immersed in 4% PFA for ~6-18 h before transfer to 30% sucrose solution in phosphate-buffered
917 saline (PBS) at 4°C. After at least 48 hr, brains were sectioned at 40 µm on a freezing sliding microtome
918 (HM430; Thermo Fisher Scientific, MA, USA) and sections stored at 4°C in 1X PBS. For
919 immunohistochemistry, sections were blocked in PBS containing 0.3% Triton X-100 (PBS-T; Sigma-
920 Aldrich, MO, USA) with 3% normal donkey serum (NDS; Jackson ImmunoResearch, PA, USA) for 30-
921 60 min at room temperature. This was followed by incubation in primary antibody solution (chicken anti-
922 TH (1:1000; AB9702; EMD Millipore, MA, USA) in 0.3% PBS-T with 3% NDS) overnight at 4°C. Sections

923 were then washed in 1X PBS four times (10 min each) before incubation in secondary antibody solution
924 containing donkey anti-chicken 488 or 647 (1:1000; Jackson Immunoresearch, PA, USA) and a DNA-
925 specific fluorescent probe (DAPI; 1:50000; Invitrogen, Thermo Fisher Scientific, MA, USA) in 0.2% PBS-
926 T with 3% NDS for 1.5-2 hr at room temperature. Sections were again washed four times in 1X PBS
927 (10 min each) before being mounted on glass slides and coverslipped using warmed PVA-DABCO
928 (Sigma-Aldrich, MO, USA).

929 Images were captured on a laser scanning confocal microscope (Olympus FV1000, Olympus,
930 PA, USA) using Fluoview software version 4.0 (Olympus, PA, USA). Images were collected through a
931 10X/0.40 NA objective for injection site and optic fiber placement verification, a 20X/0.75 objective for
932 terminal fluorescence quantification, and an oil-immersion 40X/1.30 NA objective for neurobiotin-filled
933 neurons and RNAscope analysis (see individual Methods sections for more detail). FIJI ¹²¹, CellProfiler
934 3.1 (Broad Institute, MA, USA)¹²², and Adobe Photoshop CC (Adobe Systems Incorporated, CA, USA)
935 were used for subsequent image processing and analysis.

936 ***Downstream fluorescence quantification***

937 In DAT::Cre mice, AAV₅-EF1 α -DIO-ChR2-eYFP (300 nL) was injected into the DRN (ML:1.20,
938 AP:-4.10, DV:-2.90; needle at a 20° angle from the midline, bevel facing medial) or VTA (ML:0.85, AP:-
939 2.70, DV:-4.50), and after 8 weeks mice underwent perfusion-fixation. Brains were subsequently
940 sectioned at 40 μ m, processed with immunohistochemistry for TH and DAPI, and serial z-stack images
941 (3 μ m optical thickness) collected at 20X on a confocal microscope. (See '*Immunohistochemistry and*
942 *confocal microscopy*' section above for details). A maximum projection was generated in FIJI and
943 background subtraction based on the 'rolling ball' algorithm (radius = 50 pixels) was applied to correct
944 for uneven illumination. The appropriate brain atlas slice ^{123,124} was overlaid onto the fluorescent image
945 using the BigWarp plugin (<https://imagej.net/BigWarp>) ¹²⁵ in FIJI, by designating major anatomical
946 landmarks based on DAPI staining and TH expression. Regions of interest (ROIs) were then annotated
947 from the overlaid atlas, and mean fluorescence within each ROI quantified using FIJI. The PFC was
948 examined from AP: 2.22 to 1.34, the striatum from AP 1.70 to 0.74, the BNST from AP 0.37 to -0.11,
949 the CeA from AP -0.82 to -1.94, and the amygdala from AP -0.82 to -2.92. Average images in Fig. 3a,
950 3e, 3i and S1h were created by aligning individual images (from the middle AP region of the BNST,
951 CeA, or BLP), using the line ROI registration plugin (https://imagej.net/Align_Image_by_line_ROI)
952 in FIJI. An average projection was then performed across all images and the 'royal' LUT applied to
953 visualize relative fluorescence intensity.

954 ***Retrograde tracing and intersectional viral expression***

955 C57BL/6 mice were injected with 150-250 nL CTB conjugated to Alexa Fluor-555 (CTB-555) or
956 Alexa Fluor-647 (CTB-647; Molecular Probes, OR, USA ¹²⁶) in two of three locations: the BNST
957 (ML:1.10, AP:0.50, DV: -4.30; needle bevel facing back), CeA (ML:2.85, AP: -1.20; DV:-4.75; needle
958 bevel facing back), or BLP (ML:3.35, AP:-2.20, DV:-5.25; needle bevel facing back). To assess
959 retrograde CTB co-expression following injection of both fluorophore-conjugates of CTB into the same
960 region (Fig. S4a-c), injections were either performed sequentially, or CTB-555 and CTB-647 were mixed
961 prior to a single injection. After 7 days to allow for retrograde transport, mice were deeply anaesthetized
962 with sodium pentobarbital (200 mg/kg) and perfused-fixed for subsequent histology. Brain sections
963 containing injection sites and the DRN were prepared at 40 μ m and processed with
964 immunohistochemistry for TH and DAPI. (See '*Immunohistochemistry and confocal microscopy*' section
965 above for details). CTB injection sites were verified with images acquired on a confocal microscope

966 through a 10X objective (serial z-stack with 5 μm optical thickness) and images of the DRN were
967 acquired through a 40X objective (serial z-stack with 3 μm optical thickness). DRN cells co-expressing
968 CTB and TH were counted manually using the ROI 'point' tool in Fluoview software version 4.0
969 (Olympus, PA, USA). Counted files were imported into FIJI, and images overlaid onto the appropriate
970 brain atlas image of the DRN using the BigWarp plugin (<https://imagej.net/BigWarp>)¹²⁵. The x-y
971 coordinates of counted/marked CTB+/TH+ cells were extracted using the 'Measure' function in FIJI.
972 These coordinates were then used to generate heatmaps of cell location (Fig. 2e-f) by creating a 2D
973 histogram using the Matplotlib package ¹²⁷ in Python .

974 Intersectional labelling of the dopaminergic projection from the DRN to the CeA was achieved
975 by injecting HSV-LS1L-mCherry-IRES-flpo (300 nL) into the CeA (ML:2.85, AP:-1.45, DV:-4.55; needle
976 bevel facing medial) and AAV₅-fDIO-eYFP (300 nL) into the DRN (ML:1.20, AP:-4.10, DV:-2.90; needle
977 at a 20° angle from the midline, bevel facing medial) of a DAT::Cre mouse. After 8 weeks, mice were
978 perfused-fixed with 4% PFA, and the brain sectioned on a freezing microtome at 40 μm before
979 immunohistochemical processing with TH and DAPI. Images of eYFP-expressing cells in the DRN and
980 terminals in the CeA and BNST were captured on a confocal microscope through a 20X objective with
981 a serial z-section thickness of 3 μm .

982 ***Behavioral assays and optogenetic manipulations***

983 DAT::Cre mice were injected with 300 nL AAV₅- EF1 α -DIO-ChR2-eYFP or AAV₅-EF1 α -DIO-
984 eYFP in the DRN (ML:1.20; AP:-4.10; DV:-2.90; needle at a 20° angle from the right side, bevel facing
985 medial) and optic fibers (300 μm core, NA=0.37; Thorlabs, NJ, USA), held within a stainless steel ferrule
986 (Precision Fiber Products, CA, USA), were implanted unilaterally or bilaterally over the BNST (unilateral:
987 ML:1.10, AP:0.40, DV:-3.50; bilateral: ML:1.65, AP:0.40, DV:-3.35; 10° angle from midline), CeA
988 (ML:2.85, AP:-1.35, DV:-4.00), or BLP (ML:3.30, AP:-2.20, DV:-4.30). Behavioral experiments
989 commenced 7-8 weeks following surgery. Mice were handled and habituated to patch cable connection
990 once per day for at least 3 days before beginning optical manipulations. Behavioral testing was
991 performed in dimly-lit soundproofed room during the mice's active dark phase (~10am-5pm). On each
992 testing day, mice were given at least 1 hr to acclimate to the testing room before experiments began.
993 For optical manipulations, optic fiber implants were connected to a patch cable via a ceramic sleeve
994 (Precision Fiber Products, CA, USA), which itself was connected to a commutator (rotary joint; Doric,
995 Québec, Canada) using an FC/PC adapter, to permit uninhibited movement. The commutator, in turn,
996 was connected via a second patch cable (with FC/PC connectors) to a 473 nm diode-pumped solid
997 state (DPSS) laser (OEM Laser Systems, UT, USA). To control the output of the laser, a Master-8 pulse
998 stimulator (AMPI, Israel) was used, and the light power set to 10 mW.

999 Tube test: Cages of mice (same-sex groups of 2-4) were assayed for social dominance using
1000 the tube test ^{61,62}. Mice were individually trained to pass through a clear Plexiglas tube (30 cm length,
1001 3.2 cm inner diameter) over 4 days. Each training trial involved releasing the mouse into the tube from
1002 one end, and ensuring it traveled through and out the other side. Mice which attempted to reverse or
1003 were reluctant to exit at the other end of the tube were gently encouraged forwards by light pressure
1004 from a plastic stick pressing on their hind region. Between trials mice freely explored the open arena
1005 outside tube (76 x 60 cm) for ~30-60 s. Mice performed 8 training trials (4 from each end) on days 1
1006 and 2, and 3 trials (alternating ends) on days 3 and 4. On days 5-8 mice competed against cagemates
1007 in a round-robin design. For each contest, mice were released simultaneously into opposite ends of the
1008 tube so that they met face-to-face in the center of the tube. The mouse which retreated from the
1009 confrontation was designated as the 'loser' and his opponent designated the 'winner'. Across testing

1010 days, the side from which animals were released and the order in which they were tested against
1011 cagemates was counterbalanced. An animal's 'relative dominance' score reflected their proportion of
1012 'wins' across all contests from 3-4 days of testing.

1013 Open field test (OFT): The open field was composed of a square arena (51 x 51 cm) made of
1014 transparent Plexiglas with 25 cm high walls. Mice freely explored the arena for 15 min, and blue light (8
1015 pulses with 5 ms pulse-width, at 30 Hz, every 5 s) was delivered during the middle 5 min epoch of the
1016 session. Animals were recorded using a video camera positioned above the arena, and Ethovision XT
1017 software used to track mouse location (Noldus, Netherlands). To assess anxiety-related behavior, for
1018 analysis, the chamber was divided into a 'center' square region and a 'periphery', with equal area.

1019 Three-chamber sociability assay: The apparatus consisted of a 57.5l x 22.5w x 16.5h cm
1020 chamber, with transparent Plexiglas walls and opaque grey plastic floors. The chamber was divided into
1021 unmarked left and right compartments (each 23 x 22.5 cm) and a smaller center compartment (11.5 x
1022 22.5 cm). An upturned wire mesh cup was placed in the left and right compartments. Each mouse first
1023 underwent a habituation session (10 min) where they freely explored the chamber. They were then
1024 briefly (~1 min) confined to the center compartment by the insertion of clear Plexiglas walls, while a
1025 novel object was placed under one of the two upturned cups, and a juvenile C57BL/6 mouse (3.5-5
1026 weeks of age) was placed under the other upturned cup. The mice were then allowed to freely explore
1027 the chamber for a further 10 min. The task was repeated on the second day, with the chamber rotated
1028 by 90° relative to external spatial cues, and with a different novel object and novel juvenile mouse. The
1029 10 min test epoch was paired with blue light delivery (8 pulses with 5 ms pulse-width, at 30 Hz, every 5
1030 s) on one of the two days, counterbalanced across animals. Mice were excluded if they showed a strong
1031 preference (>70% time spent) for one side of the chamber in the habituation phase, or if they spent
1032 more than 1 min on top of the upturned cups during any session. Animals were recorded using a video
1033 camera positioned above the chamber and movement tracked using Ethovision XT (Noldus,
1034 Netherlands). The social:object ratio reflected the time spent in the 'social' side of the chamber
1035 (containing a novel juvenile mouse) divided by the time spent in the 'object' side of the chamber
1036 (containing a novel object).

1037 Juvenile intruder assay: Mice were tested individually in their home cage. They freely explored
1038 alone for 5 min after which a novel juvenile mouse was placed in the cage for a further 3 min. The task
1039 was repeated on the second day with a different novel juvenile mouse. One of the two sessions was
1040 paired with blue light delivery (8 pulses with 5 ms pulse-width, at 30 Hz, every 5 s) which commenced
1041 after 2 min and continued until the end of the task (6 min total). The behavior of the mouse during the
1042 3 min with the juvenile was scored manually using ODLog software (Macropod Software, Australia).
1043 Video files were scored twice (by two different observers, blinded to the experimental conditions) and
1044 the average of their counts was used for analysis. (See also '*First order Markov analysis*' section).

1045 Elevated plus maze (EPM): The EPM was made of grey plastic and consisted of two closed
1046 arms (30l x 5w x 30h cm) and two open arms (30l x 5w cm), radiating at 90° from a central platform (5
1047 x 5 cm) and raised from the ground by 75 cm. Mice freely explored for 15 min, with blue light (8 pulses
1048 with 5 ms pulse-width, at 30 Hz, every 5 s) delivered during the middle 5 min epoch of the session. A
1049 video camera position above the EPM was used to record animals, and movement was tracked using
1050 Ethovision XT (Noldus, Netherlands).

1051 Real-time place preference (RTPP): Mice were placed in a 52l x 52w x 26.5h cm transparent
1052 Plexiglas chamber, with clear panels separating left and right sides to leave a 11.5 cm gap for mice to

1053 pass through. Mice freely explored for 30 min, during which entry into one side of the chamber resulted
1054 in delivery of blue light (15 pulses with 5 ms pulse-width, at 30 Hz, every 5 s), which continued until
1055 mice exited the zone. Entry into the opposite side did not result in blue light delivery. The side paired
1056 with blue light delivery was counterbalanced across animals. A video camera positioned above the
1057 arena recorded animals, and mouse movement was tracked using Ethovision XT (Noldus, Netherlands).

1058 Intra-cranial self-stimulation (ICSS): Mice were food deprived for 16-20 hr prior to each day of
1059 ICSS, in order to encourage behavioral responding. Testing was conducted in an operant chamber
1060 (Med Associates, VT, USA) within a custom sound-attenuating outer box. The operant chamber
1061 contained two illuminated nose-poke ports, each with an infrared beam, and a cue light positioned above
1062 each port. White noise was delivered continuously throughout the session, and successful nose-pokes
1063 (signaled by a beam break) resulted in an auditory tone (1 s duration, 1 or 1.5 kHz) and illumination of
1064 the respective cue light. A nose-poke at the 'active' port also triggered delivery of blue light (90 pulses
1065 with 5 ms pulse-width, at 30 Hz) while a nose-poke at the 'inactive' port did not trigger light delivery.
1066 The physical location of the active and inactive nose-poke ports, and the auditory tone frequency
1067 associated with each port, was counterbalanced across animals. On day 1 (training), mice completed
1068 a 2 hr session in the operant chamber in which both nose-poke ports were baited with a small amount
1069 of palatable food, in order to encourage investigation. On day 2 (testing), mice completed an identical
1070 2 hr session, except the nose-poke ports were not baited. Nose-poke activity was recorded with MedPC
1071 software (Med Associates, VT, USA) and analyzed using MATLAB (Mathworks, MA, USA). Only data
1072 from day 2 was used for analysis.

1073 Analysis of baseline behavior: The baseline behavior of all mice (i.e. without stimulation) was
1074 evaluated to uncover any relationships between specific types of behavior assessed in different tasks.
1075 These analyses used relative dominance from the tube test, the first 5 min of the OFT and EPM, and
1076 the OFF trial from the three-chamber sociability and juvenile intruder assays. Correlation matrices were
1077 generated in GraphPad Prism 8 (GraphPad Software, CA, USA) to show the Pearson's correlation
1078 coefficient for each pair of variables.

1079 Dimensionality reduction was performed on baseline behavior data using principal component
1080 analysis (PCA) with the scikit-learn module ¹²⁸ in Python. The eight input measures from behavioral
1081 assays were (1) percent time moving in the OFT, (2) time in the center of the OFT, (3) time in the open
1082 arms of the EPM, (4) social:object ratio in the three-chamber assay, and (5) time spent face sniffing, (6)
1083 anogenital sniffing, (7) rearing, and (8) grooming in the juvenile intruder assay. The data was first
1084 normalized to generate a covariance matrix and then the first 5 PCs were extracted. Relative dominance
1085 was concatenated with the resulting PC values for each mouse to color-code individual points in the
1086 PC1 vs PC2 plot.

1087 First order Markov analysis: Behavioral videos from the juvenile intruder assay were manually
1088 annotated so that each second of the 180 s session was assigned a code(s) from 15 behavioral
1089 categories:

- 1090 - Social behaviors: face sniff (reciprocated), face sniff (non-reciprocated), flank sniff,
1091 anogenital sniff (reciprocated), anogenital sniff (non-reciprocated), close follow, approach,
1092 dominant climb, attack.
- 1093 - Nonsocial behaviors: groom, dig, rear, climb, still, ambulate.

1094 If more than one behavior occurred during a 1 s period, multiple behaviors were assigned to that
1095 second (up to a maximum of 3) to ensure all behavioral transitions were included. We considered two

1096 Markov models – one 15-state model and one 2-state model, in which behaviors were assigned to either
 1097 the ‘social’ or ‘nonsocial’ categories. For each animal, we created a transition probability matrix from
 1098 each sequence by counting the number of transitions that occurred and dividing by the total number of
 1099 occurrences of that behavior. To compute the overall transition probability matrix for the eYFP and
 1100 ChR2 groups, we took the mean of the transition probability across all individuals in that group.
 1101 Difference scores between the stimulation OFF and ON sessions were calculated by taking the
 1102 difference across pairs of transition probability matrices corresponding to each individual, then
 1103 calculating the mean across eYFP or ChR2-expressing mice.

1104 To verify that a first order Markov model was an appropriate fit for our data we computed the log
 1105 likelihood chi squared statistic ¹²⁹:

$$1106 \quad G = 2 \sum_j \sum_i O_{ij} \ln \frac{O_{ij}}{E_{ij}},$$

1107 where $O_{ij} \geq 0$ is the observed number of transitions from state i to j , $E_{ij} \geq 0$ is the expected number of
 1108 transitions from state i to state j assuming a zeroth order Markov (i.e., no time dependence). We found
 1109 that G was statistically significant for all subjects in both the 15 state and 2 state models, thus rejecting
 1110 the null hypothesis of randomly transitioning between states.

1111 We also tested whether a non-stationary model was a better fit for the data than a stationary model. To
 1112 do this, we divided each subject’s behavioral sequence into two segments of equal duration and
 1113 computed transition probability matrices for each segment. We then computed a variation on the
 1114 likelihood ratio chi square statistic ¹²⁹:

$$1115 \quad LRX = 2 \sum_s \sum_j \sum_i f_{ijs} \ln \frac{\bar{p}_{ijs}}{p_{ij}},$$

1116
 1117 where s represents the segment, p_{ij} is the probability of transition from state i to j taken over the entire
 1118 sequence, \bar{p}_{ijs} is the probability of transition from i to j for each segment, and f_{ijs} is the number of
 1119 transitions from state i to j for each segment. Since not all subjects had a significant difference, we
 1120 determined that a stationary model was the most appropriate model to fit all our data.

1121 ***Ex vivo electrophysiology***

1122 DAT::Cre mice received an injection of 300 nL AAV₅-DIO-ChR2-eYFP in the DRN (ML:1.20,
 1123 AP:-4.10, DV:-2.90; needle at a 20° angle from the midline, bevel facing medial), and after at least 8
 1124 weeks for transgene expression, mice were deeply anaesthetized with sodium pentobarbital (200
 1125 mg/kg) or euthasol (150 mg/kg; IP). They were then transcardially perfused with ice-cold (~4°C)
 1126 modified artificial cerebrospinal fluid (ACSF; composition in mM: NaCl 87, KCl 2.5, NaH₂PO₄*H₂O 1.3,
 1127 MgCl₂*6H₂O 7, NaHCO₃ 25, sucrose 75, ascorbate 5, CaCl₂*2H₂O 0.5, in ddH₂O; osmolarity 320-330
 1128 mOsm, pH 7.30-7.40), saturated with carbogen gas (95% oxygen, 5% carbon dioxide) before the brain
 1129 was rapidly and carefully extracted from the cranial cavity. Thick coronal (300 μm) slices containing the
 1130 BNST, CeA, BLP, and DRN were prepared on a vibrating blade vibratome (VT1200; Leica Biosystems,
 1131 Germany), in ice-cold modified ACSF saturated with carbogen gas. Brain slices were hemisected with
 1132 a scalpel blade before transfer to a holding chamber containing ACSF (composition in mM: NaCl 126,

1133 KCl 2.5, NaH₂PO₄*H₂O 1.25, MgCl₂*6H₂O 1, NaHCO₃ 26, glucose 10, CaCl₂*H₂O 2.4; osmolarity
1134 298-302 mOsm, pH 7.30-7.40) saturated with carbogen, in a warm water bath (~30°C).

1135 Electrophysiological recordings were commenced after the slices had rested for at least 45 min.
1136 During recording, the brain slice was maintained in a bath with continuously perfused ACSF, saturated
1137 with carbogen, at 31±1°C using a peristaltic pump (Minipuls3; Gilson, WI, USA). Slices were visualized
1138 through an upright microscope (Scientifica, UK) equipped with infrared-differential interference contrast
1139 (IR-DIC) optics and a Q-imaging Retiga Exi camera (Q Imaging, Canada). In the BNST, CeA, and BLP,
1140 recordings were performed in the region containing fluorescent DRN^{DAT} terminals (expressing ChR2-
1141 eYFP) with neurons visualized through a 40X/0.80 NA water immersion objective. Terminal expression
1142 was confirmed by brief illumination from a 470 nm LED light source (pE-100; CoolLED, NY, USA)
1143 combined with the appropriate filter set. Borosilicate glass capillaries were shaped on a P-97 puller
1144 (Sutter Instrument, CA, USA) to produce pipettes for recording that had resistance values of 3.5-5
1145 MOhm when filled with internal solution (composition in mM: potassium gluconate 125, NaCl 10, HEPES
1146 20, MgATP 3, and 0.1% neurobiotin, in ddH₂O (osmolarity 287 mOsm; pH 7.3). Whole-cell patch-clamp
1147 recordings were made using pClamp 10.4 software (Molecular Devices, CA, USA), with analog signals
1148 amplified using a Multiclamp 700B amplifier, filtered at 3 kHz, and digitized at 10 kHz using a Digidata
1149 1550 (Molecular Devices, CA, USA). A 5 mV, 250 ms hyperpolarizing step was used to monitor cell
1150 health throughout the experiment, and recordings were terminated if significant changes (>20%)
1151 occurred to series resistance (R_s), input resistance (R_{in}), or holding current.

1152 Passive cell properties (capacitance, membrane resistance) were estimated from the current
1153 response to hyperpolarizing 5 mV, 250 ms steps, delivered in voltage-clamp from a holding potential of
1154 -70 mV, using custom MATLAB code written by Praneeth Namburi, based on MATLAB implementation
1155 of the Q-Method¹³⁰. To examine the membrane potential response to current injection, cells were
1156 recorded in current-clamp mode, and a series of 1 s steps were delivered, in 20 pA increments, from -
1157 120 pA to 260 pA. The voltage sag amplitude (attributable to the hyperpolarization-activated cation
1158 current; I_h) was measured as the difference between the peak instantaneous and steady-state
1159 membrane potential elicited during a -120 pA step (see Fig. 4I). The ramp ratio was calculated by
1160 dividing the average membrane potential between 900-1000 ms by the membrane potential between
1161 100-200 ms following step onset, using the largest current step that elicited a subthreshold response
1162 (i.e. did not evoke action potentials). The firing delay was taken as the time between current step onset
1163 and the first elicited action potential, on delivery of the first current step that was elicited a
1164 suprathreshold response (i.e. rheobase current). The max instantaneous firing frequency (max freq._{inst})
1165 was taken as the maximum firing frequency attained during the first 100 ms of the depolarizing current
1166 steps.

1167 To photostimulate ChR2-expressing DRN^{DAT} terminals in the BNST, CeA, and BLP, 470 nm light
1168 was delivered through the 40X/0.8 NA objective from an LED light source (pE-100; CoolLED, NY, USA).
1169 Neurons were recorded at their resting membrane potential in current-clamp mode, and 470 nm light (8
1170 pulses at 30 Hz, 5ms pulse-width) was delivered every 30 s. In a minority of cells which showed
1171 spontaneous activity at the resting potential, negative current was injected to hold the cell at a
1172 subthreshold potential (typically ~-60 mV). The peak amplitude of the optically-evoked excitatory post-
1173 synaptic potential (EPSP) or trough amplitude of the inhibitory post-synaptic potential (IPSP) was
1174 measured from the average trace using Clampfit 10.7 (Molecular Devices, CA, USA), using the 5 s prior
1175 to stimulation as baseline. Tau for the decay phase of the IPSP was estimated by fitting the IPSP with
1176 a single exponential, from the IPSP trough until return to baseline. Total voltage area was calculated

1177 from 0-5.5 s following the onset of the first light pulse. In cells where optical stimulation evoked only an
1178 EPSP the response was classed as an 'excitation', only an IPSP was classed as an 'inhibition', and a
1179 combined optically-evoked EPSP and IPSP was classed as 'mixed'. To assess the effect of
1180 photostimulation on firing activity, constant positive current was injected to elicit consistent spontaneous
1181 action potentials, and 470 nm light (8 pulses at 30 Hz, 5 ms pulse-width) was delivered every 30 s. The
1182 interevent interval (IEI) between action potentials was calculated for 5 s before and 5 s after the first
1183 pulse of blue light using Clampfit 10.7 (Molecular Devices, CA, USA). A decrease in IEI (indicating an
1184 increase in firing rate) was classed as an 'excitation' and an increase in IEI (indicating a decrease in
1185 firing rate) was classed as an 'inhibition'.

1186 Following recording, images showing the location of the recording pipette within the slice were
1187 captured through a 4X/0.10 NA objective. Images were subsequently overlaid onto the appropriate brain
1188 atlas image^{123,124}, recorded cell locations were annotated, and then converted into x-y coordinates in
1189 FIJI. Python was used to generate a scatter plot of cell location, with points color-coded by the overall
1190 membrane potential response to photostimulation (Fig. S6a-c).

1191 Unsupervised agglomerative hierarchical clustering was used to classify cells according to their
1192 baseline electrophysiological properties. This approach organizes objects (in this case cells) into
1193 clusters, based on their similarity. The electrophysiological properties used as input features for
1194 clustering CeA cells were ramp ratio, max firing frequency, firing delay, and voltage sag, which are
1195 characteristics that have been previously shown to distinguish between subtypes of CeA neuron¹⁰³.
1196 For clustering BLP cells, we replaced ramp ratio with capacitance, as this measure is often used to
1197 distinguish between pyramidal neurons and GABAergic interneurons, which are the two main cell types
1198 in this region. Data for each cell property was max-min normalized to produce a $4 \times n$ matrix of input
1199 features (where n = total number of cells). Clustering was performed using the 'linkage' function of SciPy
1200¹³¹ in Python, using Ward's linkage method¹³² and Euclidean distance. Briefly, this approach begins
1201 with each cell assigned to a single cluster. Cells that are in closest proximity (i.e. have highest similarity)
1202 are then linked to form a new cluster. Then the next closest clusters are linked, and so on. This process
1203 is repeated until all cells are included in a single cluster. The output of this analysis is plotted as a
1204 hierarchical tree (dendrogram), in which each cell is a 'leaf' and the Euclidean distance on the y-axis
1205 indicates the linkage between cells (larger distance indicates greater dissimilarity). To annotate the
1206 photostimulation response of cells on the dendrogram (Fig. 4n, 4p, and S6m), the response was
1207 designated as 'excitation' if action potential IEI decreased with optical stimulation and 'inhibition' if action
1208 potential IEI increased on stimulation. If firing data was not available, cells were designated as showing
1209 an 'excitation' if only an EPSP was evoked on optical stimulation, and 'inhibition' if only an IPSP was
1210 evoked. In cells where a mixed EPSP/IPSP was elicited, the response was designated as an 'excitation'
1211 if the overall voltage area (0-5.5 s following light onset) was positive, and an 'inhibition' if the overall
1212 voltage area was negative.

1213 At the end of recording, brain slices were fixed in 4% PFA overnight, and then washed in 1X
1214 PBS (4 x 10 min each). Slices were blocked in 0.3% PBS-T (Sigma-Aldrich, MO, USA) with 3% NDS
1215 (Jackson ImmunoResearch, PA, USA) for 30-60 min at room temperature. They were then incubated in
1216 PBS-T 0.3% with, 3% NDS, and CF405- or CF633-conjugated streptavidin (1:1000; Biotium, CA, USA)
1217 for 90 min at room temperature to reveal neurobiotin labelling. Slices were finally washed four times in
1218 1X PBS (10 min each) before being mounted on glass slides and coverslipped using warmed PVA-
1219 DABCO (Sigma-Aldrich, MO, USA).

1220 ***Single molecule fluorescent in situ hybridization (smFISH) with RNAscope***

1221 C57BL/6 mice were deeply anesthetized with 5% isoflurane and brains were rapidly extracted
1222 and covered with powdered dry ice for ~2 min. Frozen brains were stored in glass vials at -80°C before
1223 sectioning at 20 µm using a cryostat (CM3050 S; Leica Biosystems, Germany) at -16°C. Coronal
1224 sections were thaw-mounted onto a glass slide, by gentle heating from the underside using the tip of a
1225 finger to encourage adhesion of the section to the slide. They were then stored at -80°C until processing.

1226 Fluorescent *in situ* hybridization (FISH) was performed using the RNAscope Multiplex
1227 Fluorescent assay v2 (Advanced Cell Diagnostics, CA, USA). The following products were used:
1228 RNAscope Multiplex Fluorescent Reagent Kit V2 (Catalog #323110), Fluorescent Multiplex Detection
1229 Reagents (#323110), target probes for *Mus musculus* genes – *Drd1a* (#406491-C1), *Drd2* (#406501-
1230 C3), *Npbwr1* (#547181-C1), and *Vipr2* (465391-C2) – and the Tyramide Signal Amplification (TSA) Plus
1231 Fluorescence Palette Kit (NEL760001KT; PerkinElmer Inc., MA, USA) with fluorophores diluted to
1232 1:1000-1:5000. The protocol was performed as recommended by the manufacturer, with some
1233 modifications to prevent tissue degradation and optimize labelling specificity in our regions of interest.
1234 Fresh frozen slices were fixed in 4% PFA for 1 hr at 4°C. Slices were dehydrated in an ethanol series
1235 (50%, 70%, 100%, and 100% ethanol, 5 min each) and then incubated in hydrogen peroxide for 8 min
1236 at room temperature. Protease treatment was omitted in order to prevent tissue degradation. Slides
1237 were then incubated with the desired probes (pre-warmed to 40°C and cooled to room temperature) for
1238 2 hr at 40°C in a humidified oven. Following washing (2 x 30 s in 1X RNAscope wash buffer), signal
1239 amplification molecules (Amp 1, 2, and 3) were hybridized to the target probes in sequential steps, with
1240 30 min incubation for Amp 1 and 2 and 15 min incubation for Amp 3 at 40°C, all in a 40°C humidified
1241 oven followed by washing (2 x 30 s in wash buffer). For fluorescent labelling of each amplified probe,
1242 slides were incubated in channel-specific HRP for 10 min, followed by incubation with TSA fluorophore
1243 (PerkinElmer, MA, USA) for 20 min, and then incubation in HRP-blocker for 10 minutes (with 2 x 30 s
1244 washes between each step). Probes for *Drd1a*, *Drd2*, *Npbwr1*, and *Vipr2* were each labelled with green
1245 (TSA Plus Fluorescein), red (TSA Plus Cyanine 3), or far red (TSA Plus Cyanine 5) fluorophores in
1246 counterbalanced combinations. Slides were then incubated in DAPI (Advanced Cell Diagnostics, CA,
1247 USA) for 10 min, washed in 1X RNAscope wash buffer, dried for 20 min, coverslipped with warmed
1248 PVA-DABCO, (Sigma-Aldrich, St. Louis, MO) and left to dry overnight before imaging.

1249 Images were captured on a confocal laser scanning microscope (Olympus FV1000; Olympus,
1250 PA, USA) using a 40X/1.30NA oil immersion objective. Serial Z-stack images were acquired using
1251 FluoView software version 4.0 (Olympus, PA, USA) at an optical thickness of 1.5 µm. All images were
1252 acquired with identical settings for laser power, detector gain, and amplifier offset. A maximum Z-
1253 projection was performed in FIJI followed by rolling ball background subtraction to correct for uneven
1254 illumination. Image brightness and contrast were moderately adjusted using FIJI, with consistent
1255 adjustments made across images for each probe-fluorophore combination. Regions of interest were
1256 annotated on each image by overlaying the appropriate brain atlas image^{123,124} with guidance from
1257 DAPI staining and using the BigWarp plugin (<https://imagej.net/BigWarp>)¹²⁵ in FIJI. These ROI outlines
1258 were used to generate binary masks in order to regionally-restrict subsequent image analysis.
1259 Automated cell identification and analysis of fluorescent mRNA labelling was performed in CellProfiler
1260¹²² using a modified version of the 'Colocalization' template pipeline (<https://cellprofiler.org/examples>).
1261 The pipeline was optimized to identify DAPI labelling (20-40 pixels in diameter), in order to define cell
1262 outlines. This was followed by identification of fluorescent mRNA puncta (2-10 pixels in diameter) for
1263 each probe. Puncta that were localized within DAPI-identified cells (classified using the 'relate objects'
1264 module) were assigned to that cell for subsequent analysis. Quantification and further analysis/data

1265 visualization was performed using a custom-written Python code. Violin plots were made using the violin
1266 plot function in the Seaborn library ¹³³ of Python (with smoothing set to 0.2), and colocalization matrices
1267 were generated using the Seaborn heatmap function.

1268 **Statistical analyses**

1269 Statistical tests were performed using GraphPad Prism 8 (GraphPad Software, CA, USA).
1270 Normality was evaluated using the D'Agostino-Pearson test, and data are expressed as mean±standard
1271 error of the mean (SEM), unless otherwise noted. Data which followed a Gaussian distribution were
1272 compared using a paired or unpaired t-test (non-directional) for two experimental groups, and a one-
1273 way or two-way ANOVA with repeated measures for three or more experimental groups. Data for two
1274 experimental groups which did not follow a Gaussian distribution were compared using a Mann-Whitney
1275 *U* test. Correlation between two variables was assessed using the Pearson's product-moment
1276 correlation coefficient. Threshold for significance was set at * $p < 0.05$, ** $p < 0.01$ and *** $p < 0.001$.

Figures

Figure 1

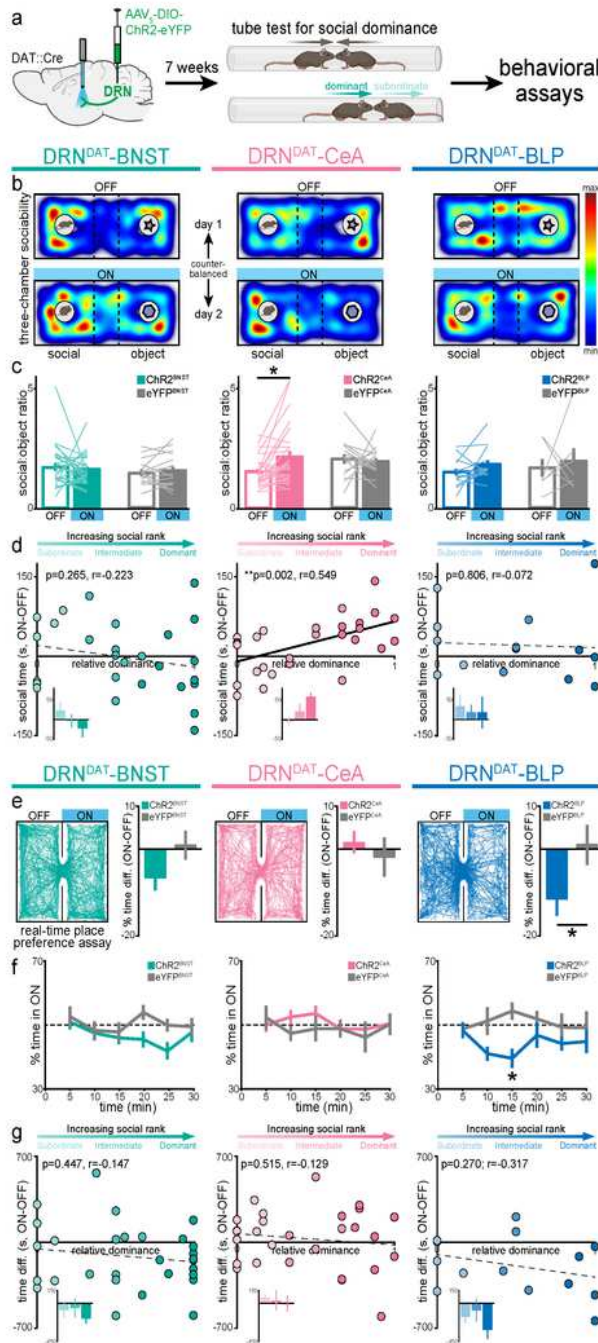


Figure 1

DRNDAT-CeA photostimulation promotes sociability but DRNDAT-BLP mediates place avoidance. a, AAV5-DIO-ChR2-eYFP or AAV5-DIO-eYFP was injected into the DRN of DAT::Cre mice and optic fibers implanted over the BNST, CeA, or BLP to photostimulate DRNDAT terminals. After >7 weeks to allow for viral

expression, cages of mice were assayed for social dominance using the tube test, prior to other behavioral tasks. b, Heatmaps showing the relative location of ChR2-expressing mice in the three-chamber sociability assay, with optic fibers located over the BNST (left), CeA (center), or BLP (right). The task was repeated across two days, with one session paired with photostimulation ('ON') and one without ('OFF'). c, Photostimulation of DRNDAT-CeA terminals (8 pulses of 5 ms pulse-width 473 nm light, delivered at 30 Hz every 5 s) in ChR2-expressing mice (ChR2CeA) increased time spent in the social zone relative to the object zone ('social:object ratio'; paired t-test: $t_{28}=2.91$; corrected for multiple comparisons across projections: $p=0.021$; $n=29$), but had no significant effect on ChR2BNST mice (paired t-test: $t_{26}=0.552$, $p=0.586$; $n=27$), ChR2BLP mice (paired t-test: $t_{13}=1.62$, $p=0.13$, $n=14$), nor eYFP mice. d, Scatter plots displaying relative dominance plotted against the change in social zone time with optical stimulation (ON-OFF), showing significant positive correlation in ChR2CeA mice (Pearson's correlation: $r=0.549$, $p=0.002$). Inset bar graphs show mean values for subordinate, intermediate, and dominant mice. e, Example tracks of ChR2BNST, ChR2CeA, and ChR2BLP mice in the real-time place preference (RTPP) assay, and bar graphs showing the difference in % time spent in the stimulated ('ON') and unstimulated ('OFF') zones. ChR2BLP mice spent proportionally less time in the stimulated zone relative to eYFPBLP mice (unpaired t-test: $t_{13}=2.13$, $p=0.0455$, $n=14$ ChR2BLP, $n=8$ eYFPBLP). f, Time spent in the ON zone across the 30 min session. ChR2BLP mice spent significantly less time in the ON zone relative to eYFPBLP mice at 15 min (repeated measures two-way ANOVA: $F_{1,20} = 4.53$, main effect of opsin $p=0.046$, Bonferroni post-hoc tests $*p<0.05$ at 15 min). g, Scatter plots showing relative dominance plotted against the difference in zone time (insets show mean values for subordinate, intermediate, and dominant mice). Bar and line graphs display mean \pm SEM. $*p<0.05$, $**p<0.01$.

Figure 2

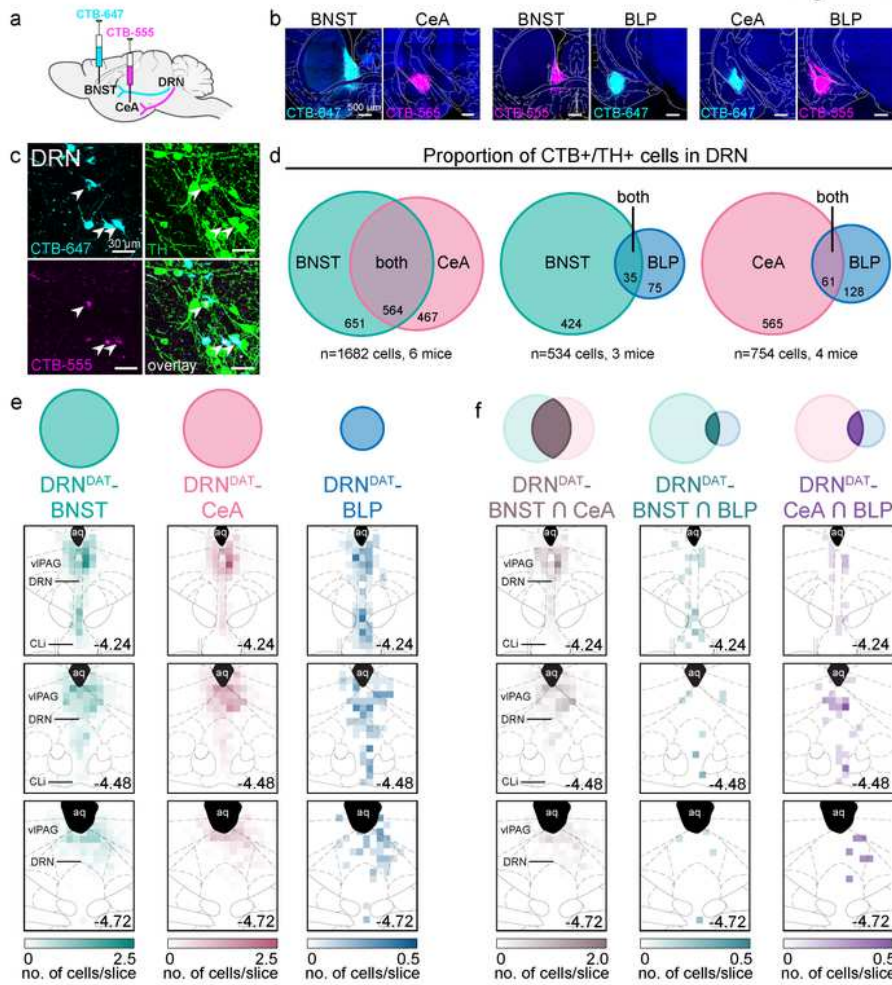


Figure 2

Collateralization of DRNDAT projections. a, The retrograde tracer cholera toxin subunit-B (CTB) conjugated to Alexa Fluor 555 (CTB-555, magenta) or Alexa-Fluor 647 (CTB-647, cyan) was injected into two downstream targets. b, Confocal images showing representative injection sites for dual BNST and CeA injections (left panels), BNST and BLP (center panels), and CeA and BLP (right panels). c, High magnification images of DRN cells expressing CTB-555 (magenta), CTB-647 (cyan), and TH (green)

following injection into the BNST and CeA. White arrows indicate triple-labelled cells. d, Venn diagrams showing the proportion of CTB+/TH+ cells in the DRN following dual injections placed in the BNST and CeA (left), BNST and BLP (center), or CeA and BLP (right). When injections were placed in the BNST and CeA, dual CTB-labelled TH+ cells constituted 46% of all BNST projectors and 55% of all CeA projectors. In contrast, when injections were placed in the BNST and BLP, or CeA and BLP, the proportion of dual-labelled cells was considerably lower (7.6% of BNST projectors and 9.7% of CeA projectors). e, Heatmaps indicating the relative density of TH+ CTB+ cells throughout the DRN/CLi for each projector population and f, dual-labelled cells. Color intensity represents average number of cells per slice. The total number of TH+ BNST and CeA projectors per slice was similar (n=27.9 BNST projectors and n=27.2 CeA projectors per slice), whereas TH+ BLP projectors were significantly fewer in number (n=6.4 BLP projectors per slice; Kruskal-Wallis statistic = 83.5, $p < 0.0001$; Dunn's post-hoc tests: BNST vs. CeA $p > 0.05$, BNST vs BLP $p < 0.001$, CeA vs BLP $p < 0.001$). TH+ BNST and CeA projectors, and dual-labelled cells, were broadly distributed throughout the DRN, vIPAG, and CLi, with a higher concentration in the dorsal aspect of the DRN, whereas BLP projectors tended to be relatively denser in ventral DRN/CLi.

Figure 3

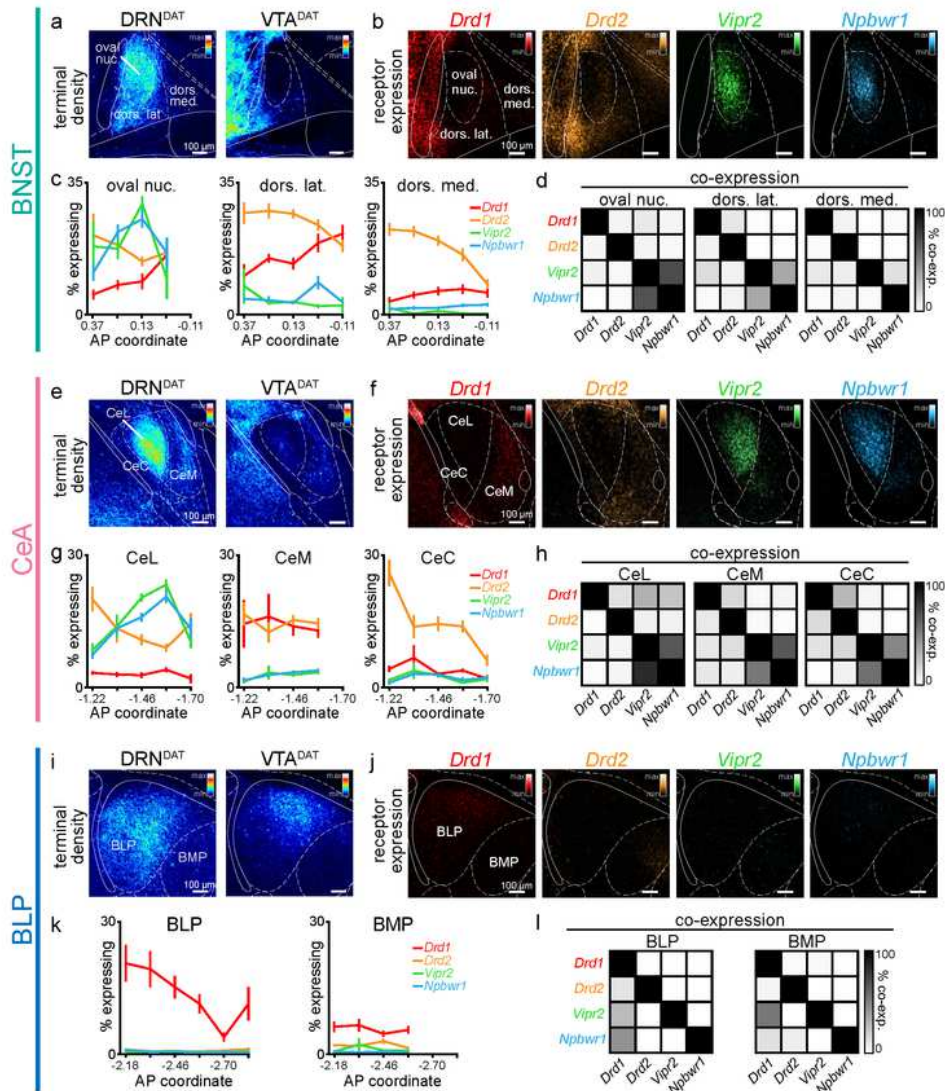


Figure 3

Spatial-segregation of dopamine and neuropeptide receptor populations within DRNDAT terminal fields. a, Average image showing terminal density in the middle anteroposterior (AP) region of the BNST, following eYFP expression in DRNDAT (left) or VTADAT (right) neurons. b, Average images showing fluorescent puncta in the BNST indicating detection of *Drd1* (red), *Drd2* (yellow), *Vipr2* (green), or *Npbwr1* (blue) mRNA transcripts. c, Line graphs showing the percent of cells expressing each receptor (≥ 5 puncta)

across AP locations for the oval nucleus, dorsolateral BNST, and dorsomedial BNST (two-way ANOVA, oval nucleus: RNA probe x AP interaction, $F_{9,160}=6.194$, $p<0.0001$, dorsolateral BNST: RNA probe x AP interaction, $F_{12,167}=3.410$, $p=0.0002$, dorsomedial BNST: RNA probe x AP interaction, $F_{12,161}=2.268$, $p=0.0110$). Drd1: $n=51,55,53$, Drd2: $n=52,55,53$, Vipr2: $n=37,39,37$, Npbwr1: $n=36,38,38$ sections, for oval nucleus, dorsolateral BNST, and dorsomedial BNST, respectively, from 4 mice. d, Matrices indicating overlap between mRNA-expressing cells: square color indicates the percent of cells expressing the gene in the column from within cells expressing the gene in the row. e, Average image showing terminal density in the middle AP region of the CeA, following eYFP expression in DRNDAT (left) or VTADAT (right) neurons. f, Average images showing fluorescent puncta in the CeA indicating mRNA expression. g, Line graphs showing the % of cells expressing each receptor (≥ 5 puncta) across AP locations for the CeL, CeM, and CeC (two-way ANOVA, CeL: RNA probe x AP interaction, $F_{12,220}=8.664$, $p<0.0001$, CeM: main effect of RNA probe, $F_{3,186}=60.30$, $p<0.0001$, CeC: RNA probe x AP interaction, $F_{12,218}=4.883$, $p<0.0001$). Drd1: $n=47,40,47$, Drd2: $n=70,55,70$, Vipr2: $n=65,57,63$, Npbwr1: $n=62,50,60$ sections, for CeL, CeM, and CeC, respectively, from 4 mice. h, Matrices indicating overlap between mRNA-expressing cells. i, Average image showing terminal density in the middle AP region of the BLP, following eYFP expression in DRNDAT (left) or VTADAT (right) neurons. j, Average images showing fluorescent puncta in the BLP indicating mRNA expression. k, Line graphs showing the percent of cells expressing each receptor (≥ 5 puncta) across AP locations for the BLP and BMP (two-way ANOVA, BLP: RNA probe x AP interaction, $F_{15,176}=2.165$, $p=0.0091$, BMP: main effect of RNA probe, $F_{3,141}=56.92$, $p<0.0001$). Drd1: $n=55,44$ Drd2: $n=59,46$ Vipr2: $n=41,33$ Npbwr1: $n=45,34$ sections, for BLP and BMP, respectively, from 4 mice. l, Matrices indicating overlap between mRNA-expressing cells. Line graphs show mean \pm SEM.

Figure 4

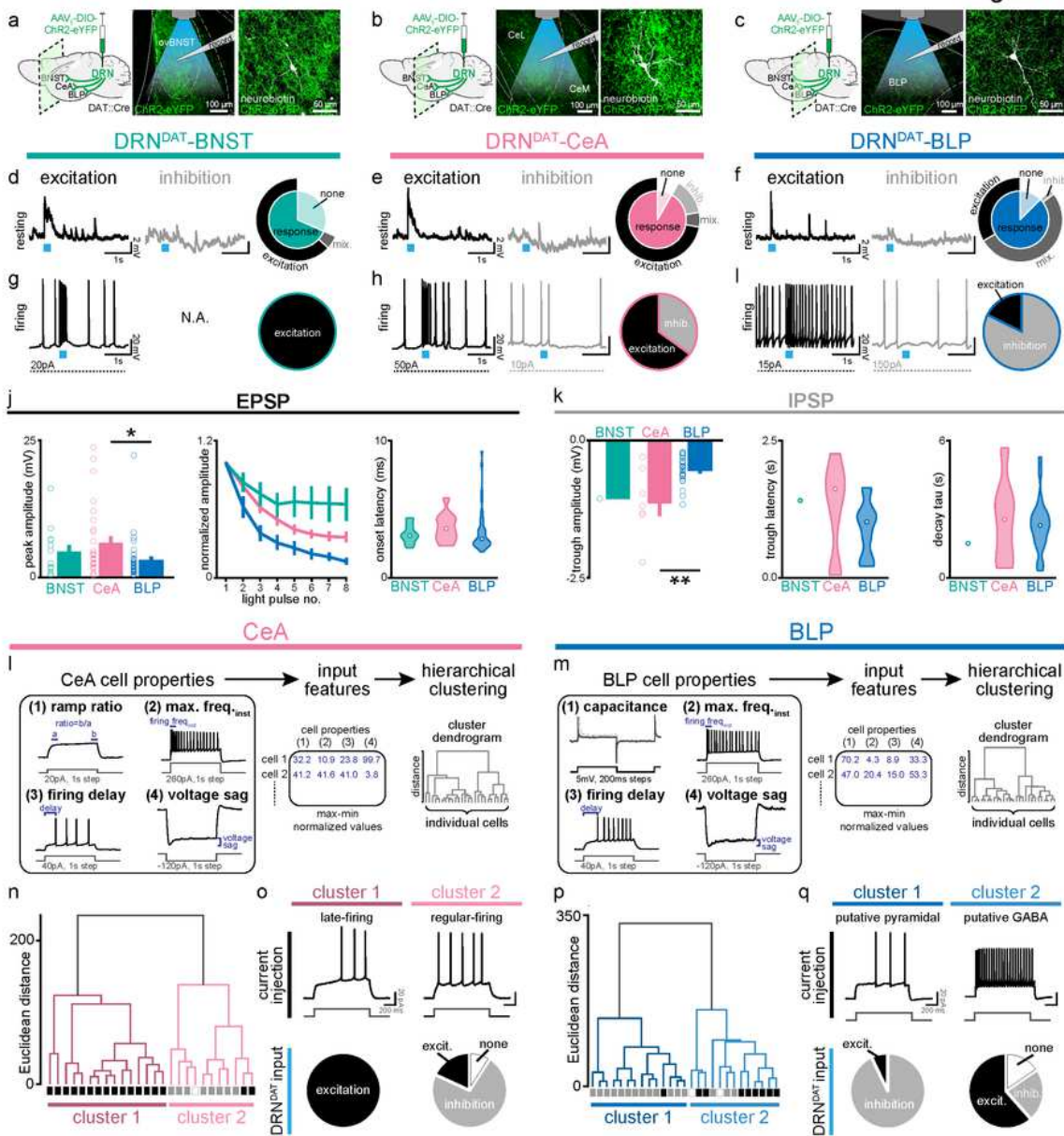


Figure 4

DRNDAT input influences downstream activity in a cell type-dependent manner. a, In mice expressing Chr2 in DRNDAT neurons, ex vivo electrophysiological recordings were made from the BNST, b, CeA, and c, BLP. d, Photostimulation of DRNDAT terminals with blue light (8 pulses delivered at 30 Hz) evoked both excitatory and inhibitory responses at resting membrane potentials in the BNST, e, CeA, and f, BLP. Traces show single sweeps and pie charts indicate proportion of cells with no response ('none'), an EPSP only

(‘excitation’), an IPSP only (‘inhibition’), or a mixed response (‘mix’). Recorded cells: BNST n=19, CeA n=36, BLP n=48, from 19 mice. g, When constant current was injected to elicit spontaneous firing, BNST cells responded to photostimulation with an increase in firing (‘excitation’), while h, CeA and i, BLP cells responded with an increase or a decrease in firing (‘inhibition’). Recorded cells: BNST n=5, CeA n=20, BLP n=17. j, Properties of the optically-evoked excitatory post-synaptic potential (EPSP) at resting membrane potentials – left: peak amplitude (Kruskal-Wallis statistic = 6.790, $p=0.0335$; Dunn’s posts-hoc tests: CeA vs BLP $p=0.0378$); middle: change in amplitude across light pulses; right: violin plots showing distribution of onset latencies (white circle indicates median). k, Properties of the optically-evoked inhibitory post-synaptic potential (EPSP) at resting membrane potentials – left: trough amplitude (one-way ANOVA, $F_{2,31}=8.150$, $p=0.0014$, CeA vs BLP: $**p=0.0014$); middle: violin plot showing latency to trough peak; right: violin plot showing tau for the current decay (white circle indicates median). Bar and line graphs display mean \pm SEM. $*p<0.05$, $**p<0.01$. l, Workflow for agglomerative hierarchical clustering of CeA neurons and m, BLP neurons. Four baseline electrical properties were used as input features, following max-min normalization (see Methods) and Ward’s method used to generate a cluster dendrogram, grouping cells based on Euclidean distance. n, Dendrogram for CeA cells indicating two major clusters, with their response to DRNDAT input indicated below each branch (excitation=black; inhibition=grey; no response=open). o, Upper panels: cluster 1 showed baseline properties typical of ‘late-firing’ neurons and cluster 2 showed baseline properties typical of ‘regular-firing’ neurons. Lower panels: pie charts showing the response of cells in each cluster to DRNDAT input. p, Dendrogram for BLP cells indicating two major clusters, with their response to DRNDAT input indicated below each branch (excitation=black; inhibition=grey; no response=open). q, Upper panels: cluster 1 showed baseline properties typical of pyramidal neurons and cluster 2 showed baseline properties typical of GABA interneurons. Lower panels: pie charts showing the response of cells in each cluster to DRNDAT input.

Supplementary Files

This is a list of supplementary files associated with this preprint. Click to download.

- [SupplementaryFigureLegends.docx](#)